MODELING THE EFFECT OF GRANULAR MEDIA ARRANGEMENTS ON STRAINS APPLIED TO AN IMPACT SURFACE USING DIGITAL IMAGE CORRELATION

A Thesis
Presented to
The Academic Faculty

by

Carlos Maximiliano Pacheco Sánchez

In Partial Fulfillment
of the Requirements for the Degree
Master of Science in the
School of Mechanical Engineering

Georgia Institute of Technology
May 2024

MODELING THE EFFECT OF GRANULAR MEDIA ARRANGEMENTS

ON STRAINS APPLIED TO AN IMPACT SURFACE USING DIGITAL IMAGE CORRELATION

Approved by:

Dr. Michael J. Leamy, Advisor
School of Mechanical Engineering
Georgia Institute of Technology

Dr. Antonia Antoniou, Advisor
School of Mechanical Engineering
Georgia Institute of Technology

Dr. Rick Neu
School of Mechanical Engineering
Georgia Institute of Technology

Date Approved: March 25th, 2024

Old folks talking ‘bout back in my day…

But homie this is my day.

To the students of the Georgia Institute of Technology

ACKNOWLEDGEMENTS

I would like to dedicate my thesis to my mom, dad, and two sisters who have always been my biggest motivators throughout my academic journey. To my parents, thank you for making sacrifices so that I was able to get opportunities to grow and learn beyond what you could. I would also like to thank my advisors, Dr. Leamy and Dr. Antoniou, for providing me with the opportunity, lab, guidance, and resources to do this research as well as Dr. Neu for being a member of my committee. Seeing as this is the conclusion of my academic career, I would like to thank all my teachers at VG, TS, NWES, SFMS, SFHS, and professors at GT. There is something I learned in every class that has shaped me into who I am today. This achievement is mine to share with you.

TABLE OF CONTENTS

LIST OF TABLES

LIST OF FIGURES

LIST OF SYMBOLS AND ABBREIVIATIONS

DIC	Digital image correlation
1D	One dimensional
2D	Two dimensional
3D	Three dimensional
PDMS	Polydimethylsiloxane
ROI	Region of interest
FPS	Frames per second
NCC	Normalized cross correlation
FA-GN	Forward additive gauss-newton method
IC-GN	Inverse compositional gauss-newton method
RG-DIC	Reliability guided DIC method
NCC	Normalized cross correlation
PLA	Polylactic acid
RRR	Granular media combination comprised of a bottom layer of 5 red granules, a middle later of 4 red granules, and a top layer of 5 red granules.
YYY	Granular media combination comprised of a bottom layer of 5 yellow granules, a middle later of 4 yellow granules, and a top layer of 5 yellow granules.
YRY	Granular media combination comprised of a bottom layer of 5 yellow granules, a middle later of 4 red granules, and a top layer of 5 yellow granules.

BBB	Granular media combination comprised of a bottom layer of 3 blue granules, a middle later of 2 blue granules, and a top layer of 3 blue granules.
v	Velocity
μ	Frictional coefficient
a_n	Dampening coefficient
τ	Time step
C_{CC}	Grayscale values at final subset points
C_{LS}	Grayscale values at current subset points
f	Reference grayscale value at specific point
g	Current grayscale value at specific point
f_m	Mean grayscale values of final reference subset
g_m	Mean grayscale values of current subset
ΔP	Change in distance between points (deformation)
Eq.	Equation
P	Point
dB	Decibel
Y	Yellow granule
B	Blue granule
R	Red granule
L	Length of granular media row in contact with polymer
n	Number of granules used
d	Diameter of granule
k	Spring Constant

$L_{c,i}$	Spring compression length at impact
L_0	Uncompressed spring length
F_{YYY}	Force impacting YYY combination
F_{RRR}	Force impacting RRR combination
h	Height
x	Spring length at given point
E	Young's modulus
℃	Celsius
%	Percent
ε_{yy}	y-direction normal strain
ε_{xx}	x-direction normal strain
ε_{xy}	Shear strain in the x-y plane
E	Energy-like quantity

SUMMARY

A series of physical experiments performed on an apparatus are presented to investigate the contact and wave propagation in granular media combinations with a flexible elastomer impact surface. The design, fabrication, and modifications of the apparatus and experimental setup are discussed in detail. Its capabilities are demonstrated by obtaining clear displacement measurements of the elastomer at maximum compression. Results between combinations are quantified and compared by calculating the strains experienced under the area of contact between the granules and the elastomer impact surface. The modification of the experimental setup allows for the recording of the area under the center, left most, and right most granules at maximum compression. A digital image correlation (DIC) technique is implemented through the ncorr software to calculate these strains using the recorded displacements of the elastomer boundary. The results gain insight into the change in strains and energy experienced based on different granule diameters used in the varying combinations. Relationships between the physical results and existing computer models are discussed.

CHAPTER 1: INTRODUCTION AND BACKGROUND

1.1 Problem, Importance, and Goals

Over the years, granular media has attracted interest in the field of acoustics for its unique properties such as nonlinear energy exchanges and break of acoustic reciprocity [1,2]. The ability to understand these properties can lead to practical engineering uses such as shock mitigation [3] and acoustic filters [4]. Much of the research performed on granular media is theoretical. Furthermore, there is a lack of physical experimental work regarding the interactions between granular media and system boundaries. Several papers discuss the creation of computer models that prove the addition of granular media can slow a transmitted wave and reduce the energy experienced by an impact surface [5]. As an extension of these findings, the physical experiments demonstrated in this paper closely replicate a computer model from Vakakis *et al*. [5] and the results are compared. Rather than looking at energy, the results in this paper focus on the strain experienced in the same granular-solid interface.

The main goal of this paper is to physically observe and establish relationships between the granular media and an applied stress wave at an impact surface. This is done by recording the movement of speckles on an elastic impact surface after an impulse force is applied to a granular media combination. A Digital Imaging Correlation (DIC) program is used to analyze the speckle pattern movement and calculate strains experienced. To the author's knowledge, there is no previous research conducted that observes the effects of granular media on an impact surface using DIC. While limited by the resources and time frame of this research, experimentally demonstrating a physical relationship between granular media and strain experienced on an impact surface provides motivation for future research in the field.

1.2 Granular Media Review

There is extensive existing research regarding the application of granular media on impact surfaces. Nesterenko's work on one-dimensional (1D) homogeneous granular chains discovered spatially localized and nonlinear solitary pulses, termed Nesterenko-solitary pulses, which are characterized by their ability to propagate through granular chains under minimal or no pre-compression. His discovery demonstrates granular media's unique tunability to energy levels due to the rapid momentum transfer [6,7]. The nonlinearity observed by Nesterenko can be attributed to the force interaction between spherical particles under compression, better known as the Hertzian Law [8]. Building upon 1D models, a study by Vakakis *et al*. extends the investigation to two-dimensional (2D) ordered granular media assemblies. The work emphasizes the absence of pre-compression and the prevalence of strong nonlinear interactions due to Hertzian contacts. A discrete element method is used to model the dynamics within these granular systems [9].

The nonlinear acoustic features of granular media, distinct from those found in linear acoustical systems, include tunable frequency pass bands and the capability for intense nonlinear energy exchanges. Previous studies have explored solitary wave tuning among the granules in 1D granular chains [10]. Furthermore, the interaction between granular media and flexible boundaries adds a layer of complexity, with the reflection and localization of solitary waves being significantly influenced by the mechanical properties of the boundary medium. The majority of the 1D and 2D granular media models use fixed boundaries [11], while few consider the effects between the granular media and the boundaries of the system. However, 1D interactions with an elastic thin plate [12] demonstrated the material properties such as the elasticity, thickness, and shape influenced wave propagation through the plate and wave reflections from the plate. Similarly, studies conducted by Potekin [13] and Zhang [14] showed

an inverse relationship between the local stiffness of granular-boundary interface and the energy transferred between the granules and a flexible boundary.

Vakakis' *et al.* work dives deeper into the nonlinear wave propagation within 2D granular media interfacing with linear elastic boundaries. There are existing numerical method models for 2D granular media; the majority of these are based strictly on axial Hertzian interactions. However, there have been several publications that highlight the rotational effects within granular media during impact have influence in the dynamics [15]. Ignoring the rotational dynamics of the granules could result in significant error as there are frictional effects and energy loss associated with the rotations [16,17,18]. Studies performed have shown the redistribution of energy through a granular system is related to the number of contact points. Plastic deformation within contact points further attributes to energy loss [19].

Bourrier used a discrete element method to predict physical processes of 2D granular media during an impact from a larger granule. It was found that different granular media particle sizes being impacted by a larger particle experience different impact processes and energy transfers. Furthermore, the wave propagation through the impacted granular media resembles a conical shape [20]. Wave transmission through granular networks have been studied by Leonard who found exponential decay in the pulse based on the number of granular branches [21]. Leonard also studied 2D wave propagation though granular media arranged hexagonal crystal lattices and found the decay a wave propagating through the granular media is related to the angle of impact [22].

Vakakis's *et al*. exploration developed a computationally efficient and robust algorithm for modeling the strongly nonlinear acoustics at granular-solid interfaces by taking into account both Hertzian interactions and tangential frictional effects within the granular media. The proposed

system has three major sources of nonlinearity: Hertzian interactions under compressive loads, collisions between granules after separation, and frictional forces due to granule rotations which occur not only within the granular media but at the boundary interfaces [5].

Vakakis *et al*. model the granular media in the model as spheres composed of steel. These granular media are hexagonally arranged and looked at in 2D. The model consists of an impact surface (plate) , fourteen total granules in a 5-4-5 arrangement, and an excitation impulse of v = 0.5 m/s. The top and bottom sides of the granular media are as to constrain the granular media from displacing laterally in respect to the impulse direction. The plate is made from steel and also constrained in the top and bottom while the right side is free to move. The area of granular media in contact with the plate is referred to as the granular-solid interface. The model applied frictional and damping coefficients to the granular media as $\mu = 0.099$ and $a_n = 6.313 * 10^{-3}$ respectively [5]. Results from the model show the transfer of energy density throughout the granular media and granular media interface for different time steps. Figure 1 depicts the energy density distribution at the granular solid boundary and within the granular media obtained from Vakakis's *et al*. computer model.

To observe the dampening features of granular media, an impulse was applied to a second (right) plate in contact with the original (left) plate and energy density measured at the plate interfaces. The snapshots of energy density distribution in the granular-solid interface and plate to plate interface are shown in Figure 1. A comparison between the energy density at the granular media interface and the plate-to-plate interface shows the granular media significantly dissipate the energy experienced by the left plate. Furthermore, waves are notably delayed when transmitted through the granular media, due to a "softening" effect in acoustics, unlike a solid plate to plate wave transmission. Another result observation within the granular media model is

that at maximum compression the energy density is greater in the interface between the outer granules compared to the center granule. The area over which the energy density is experienced is also larger. Vakakis *et al*. concludes by emphasizing that even accounting for rotational effects, energy might be dissipated in directions orthogonal to the axial impact direction.

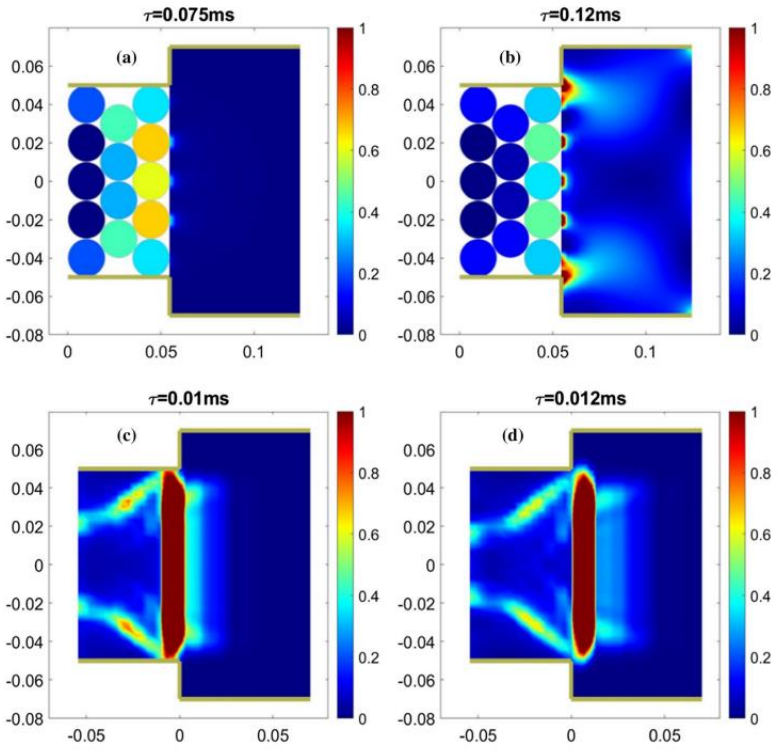

Figure 1 - Snapshots of energy density in the granular medium model and plate-to-plate model at max compression, $\tau = 0.012\ ms$ (obtained from ref.[5]).

1.3 Applications

A large majority of the interest in granular media stems from the field of acoustics. There is a possibility of widespread applications that features of granular media could create such as shock mitigation [23, 24], granular protectors [25], acoustic devices, and tunable frequency pass bands. [26]. The passive tunability feature experienced by granular media could lead to the design of

shock protection systems with the ability to self-tune their acoustics depending on the type of applied excitation [5]. Depending on the size of granular media, volume, and contact area there could be several new shock absorption engineering applications.

For instance, granular media could be used to soften impact during landing for a payload arriving on the Moon, Mars, or even on Earth. If scaled down, granular media could be implemented in shoes as a method to soften the impact experienced by a user during training or running and decrease stress on the lower body. This application could similarly be used in footwear for older individuals and those who have sensitive feet. The nature of granular media itself is an interesting concept to think about. Although the existing computer model and new experimental model proposed constrain the granular media, the possibility of implementing the granular media into flexible boundaries makes it versatile. For example, a flexible bag with granular media could be molded into the specific shape needed to protect a product during shipping. Such deformable pads have been researched in the context of applying a load to a deformable, fluid-like granular pad until it deforms into a substrate and becomes rigid [27].

Although most of these applications are far from development, the author hopes that demonstrating a physical relationship between granular media and reduced stress incites researchers to begin physically experimenting granular media effects on boundaries in different scenarios. Varying diameters, materials, shapes, direction of impact, boundaries, volume, area in contact, and so many more variables lead to endless possibilities for innovation.

1.4 DIC Background

Digital Image Correlation (DIC) is an optical technique used to measure the displacement and strain on a specimen under applied forces. The technique consists of capturing a series of

images of the specimen during deformation and comparing them to an undeformed image. An algorithm collects the image data, tracks the surface pattern movement, and calculates the displacements and strains shown in Figure 2. The algorithm correlates specific points on the surface between the undeformed and deformed object by comparing grayscale intensity patterns. The correlation of the points is analyzed in subsets, broken down areas within the image, which can be adjusted to receive detailed results or computational efficiency. There are several transformation equations, correlation criteria, and optimization methods such as the Gauss-Newton method which are implemented in the algorithm.

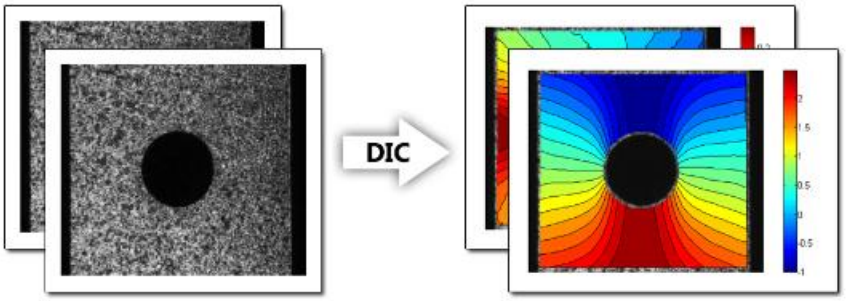

Figure 2 – Visual aid showcasing DIC inputs and outputs.

Ncorr Software is a MATLAB based software through which 2D-DIC analysis is implemented [28]. There are several steps taken when conducting DIC analysis which are more thoroughly explained in the DIC Parameters section of this report. Parameters such as subset size, number of cores, region of interest, and strain radius are user adjusted and affect results and computational time. The results from the DIC analysis yield displacement experienced throughout the region of interest of the object which are illustrated in plots for visual purposes.

An important concept of DIC is the idea of subsets; subsets are smaller sub sections of the image being analyzed. Points within the subset are 2D coordinates, which can be defined in a vector as:

$$\xi_{ref_c} + w(\Delta\xi_{ref}; p_{rc}) = \begin{Bmatrix} x^T_{ref_c} \\ y^T_{ref_c} \\ 1 \end{Bmatrix} + \begin{bmatrix} 1+\frac{du}{dx_{rc}} & \frac{du}{dy_{rc}} & u_{rc} \\ \frac{dv}{dx_{rc}} & 1+\frac{dv}{dy_{rc}} & v_{rc} \\ 0 & 0 & 1 \end{bmatrix} * \begin{Bmatrix} \Delta x^T_{ref_c} \\ \Delta y^T_{ref_c} \\ 1 \end{Bmatrix} \quad (1)$$

where x_{ref} and y_{ref} are the x and y coordinates of an initial reference subset point, $x_{ref,c}$ and $y_{ref,c}$ are the x and y coordinates of the center of the initial reference subset, ξ is an augmented vector containing the x and y coordinates of subset points, and $\frac{du}{dy}, \frac{dv}{dy}$ and $\frac{du}{dy}, \frac{dv}{dy}$ are the distance between a subset point and the center of the subset.

Nonlinear optimization is implemented to find an accurate location of points within subsets between the undeformed and deformed images. As it is an iterative scheme, it requires an initial guess. The most common method to obtain this guess is normalized cross correlation (NCC) [29]. A correlation coefficient is calculated by comparing the grayscale values at the final subset points C_{CC} with the grayscale values at the current subset C_{LS} seen on Equations 2 and 3:

$$C_{cc} = \frac{\sum_{(i,j)\in S}(f\left(\tilde{x}_{ref_i}, \tilde{y}_{ref_j}\right) - f_m)(g\left(\tilde{x}_{cur_i}, \tilde{y}_{cur_j}\right) - g_m)}{\sqrt{\sum_{(i,j)\in S}\left[f\left(\tilde{x}_{ref_i}, \tilde{y}_{ref_j}\right) - f_m\right]^2 \sum_{(i,j)\in S}\left[g\left(\tilde{x}_{cur_i}, \tilde{y}_{cur_j}\right) - g_m\right]^2}} \quad (2)$$

$$C_{LS} = \sum_{(i,j)\in S}\left[\frac{f\left(\tilde{x}_{ref_i}, \tilde{y}_{ref_j}\right) - f_m}{\sum_{(i,j)\in S}\left[f\left(\tilde{x}_{ref_i}, \tilde{y}_{ref_j}\right) - f_m\right]^2} - \frac{g\left(\tilde{x}_{cur_i}, \tilde{y}_{cur_j}\right) - g_m}{\sum_{(i,j)\in S}\left[g\left(\tilde{x}_{cur_i}, \tilde{y}_{cur_j}\right) - g_m\right]^2}\right]^2 \quad (3)$$

where f and g are the reference and current image grayscale value at a specific point, and f_m and g_m are the mean grayscale values of the final reference and current subset found as:

$$f_m = \frac{\sum_{(i,j)\in S} f\left(\tilde{x}_{ref_i}, \tilde{y}_{ref_j}\right)}{n(S)} \tag{4}$$

$$g_m = \frac{\sum_{(i,j)\in S} g\left(\tilde{x}_{cur_i}, \tilde{y}_{cur_j}\right)}{n(S)} \tag{5}$$

Equations 2-5 are used to find the correlation coefficient for every pixel throughout the region of interest. After iterating through all the pixels, the coordinates of the highest correlation coefficient value yield the location of the current subset.

There are two main optimizations methods utilized in DIC to find the convergence of a solution. The Forward Additive Gauss-Newton Method (FA-GN) is used to find the roots of a function by determining where the norm of a gradient converges to zero. This method is commonly used throughout DIC due to its straightforward computation. In DIC, the FA-GN method updates the current solution by adding the change in deformation vectors (Δp) to the current parameters each iteration (Eq. 6). The reference subset remains undeformed while the target subset is deformed according to the previous solution estimate. Therefore, the hessian calculated must be differentiable with respect to the deformation parameters and recalculated each iteration as it is a function of the old deformation distance which can be seen on Equation 7.

$$p_{new} = p_{old} + \Delta p \tag{6}$$

$$\nabla\nabla C_{LS}(p_{old}) = \frac{d^2 C_{LS}(p_{old})}{\Delta p} \approx \frac{2}{\sum\left[g\left(\xi_{ref_c} + w(\Delta\xi_{ref}; p_{old})\right) - g_m\right]^2} \sum_{(i,j)\in S} \left[\frac{\partial}{\partial \Delta p} g\left(\xi_{ref_c} + w(\Delta\xi_{ref}; p_{old})\right)\right]\left[\frac{\partial}{\partial \Delta p} g\left(\xi_{ref_c} + w(\Delta\xi_{ref}; p_{old})\right)\right]^T \tag{7}$$

The second method used is the Inverse Compositional Gauss-Newton (IC-GN) method. This method achieves the same solution convergence but reverses the role of the reference and target subsets. Contrary to the FA-GN method, the target subset remains constant while the

reference subset is deformed in iterations. The change in deformation that the reference subset must undergo is calculated and inverted. This change in deformation is applied to the target subset which is already transformed with the deformation (because it is the deformed image). Therefore, this method avoids a direct update of the target subset every iteration. Much like in FA-GN, the hessian still needs to be calculated to find ΔP. However, the hessian is evaluated at $P = 0$; because it is evaluated at the same position every iteration, it only needs to be computed once (shown in Eq. 8). Having a constant hessian reduces the computational time per iteration and can lead to solution convergence 3 to 5 times faster than FA-GN [30].

$$\nabla\nabla C_{LS}(0) \approx \frac{dC_{LS}(0)}{d\Delta p^2} \approx \frac{2}{\sum\left[f\left(\xi_{ref_c} + w(\Delta\xi_{ref}; 0)\right) - f_m\right]^2} \sum\left[\frac{d}{d\Delta p} f\left(\xi_{ref_c} + w(\Delta\xi_{ref}; 0)\right)\right]\left[\frac{d}{d\Delta p} f\left(\xi_{ref_c} + w(\Delta\xi_{ref}; 0)\right)\right]^T \quad (8)$$

To improve accuracy and reliability of results, ncorr implements a reliability guided DIC method. (RG-DIC). Initial seeds are selected around features easily recognizable pre and post deformation. Bing Pan's reliability guided method [31] is used to obtain the full field displacements. The subsets around the seeds aid as the baseline for displacement and strain measurements for the rest of the area. These subsets are the only ones that use previously discussed methods to obtain an initial guess. After the initial seed analysis, the rest of the ROI is analyzed by prioritizing the subsets with a higher reliability score for displacement and strain calculations and using this data to analyze the rest of the neighboring subsets. If the reliability scores are low from factors such as blurry images or complex deformation in certain areas, the method will automatically adapt and change certain parameters including subset radius or step size to optimize the correlation between points within images and output better displacement and strain data.

Strains are calculated separately after the displacements have been found. The four displacement gradients shown in Equations 9-11 can be used to calculate the Green-Lagrangian strain:

$$E_{xx} = \frac{1}{2}\left(2\frac{\partial u}{\partial x} + \left(\frac{\partial u}{\partial x}\right)^2 + \left(\frac{\partial v}{\partial x}\right)^2\right) \tag{9}$$

$$E_{xy} = \frac{1}{2}\left(\frac{\partial u}{\partial y} + \frac{\partial v}{\partial x} + \frac{\partial u}{\partial x}\frac{\partial u}{\partial y} + \frac{\partial v}{\partial x}\frac{\partial v}{\partial y}\right) \tag{10}$$

$$E_{yy} = \frac{1}{2}\left(2\frac{\partial v}{\partial y} + \left(\frac{\partial u}{\partial y}\right)^2 + \left(\frac{\partial v}{\partial y}\right)^2\right) \tag{11}$$

Ncorr calculates the displacement gradients straight from the displacement fields rather than using the obtained gradients through the IC-GN method [32]. The equations for the displacement planes are:

$$u_{plane}(x,y) = a_{u,plane} + \left(\frac{\partial u}{dx_{plane}}\right)x + \left(\frac{\partial u}{dy_{plane}}\right)y \tag{12}$$

$$v_{plane}(x,y) = a_{v,plane} + \left(\frac{\partial v}{dx_{plane}}\right)x + \left(\frac{\partial v}{dy_{plane}}\right)y \tag{13}$$

The DIC algorithm stores the displacements as vector fields which are used to calculate the strains using a system of equations in the form seen on Eq. 14.

$$\begin{bmatrix} 1 & x_{ref_{first\,i}} - x_{ref_c} & y_{ref_{first\,j}} - y_{ref_c} \\ \vdots & \vdots & \vdots \\ 1 & x_{ref_{last\,i}} - x_{ref_c} & y_{ref_{last\,j}} - y_{ref_c} \end{bmatrix} \begin{Bmatrix} a_{u,plane} \\ \left(\frac{\partial u}{dx_{plane}}\right) \\ \left(\frac{\partial u}{dy_{plane}}\right) \end{Bmatrix} = \begin{Bmatrix} u^*_{rc\left(x_{ref_{first\,i}}, y_{ref_{first\,j}}\right)} \\ \vdots \\ u^*_{rc\left(x_{ref_{last\,i}}, y_{ref_{last\,j}}\right)} \end{Bmatrix} \tag{14}$$

The strain is then calculated using the displacement vectors and gradient by finding the change in distance between two points relative to the original distance. This can otherwise be pictured as the distance a speckle or point moved relative to the starting position. The strain radius is an

important feature manually adjusted to yield smooth strain gradient charts. This enables a change in spatial resolution based on strain radius chosen, with a smaller radius allowing a higher spatial resolution and detailed gradients throughout the region of interest. The advantage of using a smaller strain radius is the ability to detect localized effects throughout the object. However, having too small of a strain radius can lead to an overcrowding of localized effect and a non-cohesive image. Ncorr has a strain radius range of 0 to 50 pixels; the radius converted to mm is 0 to 0.3611mm. There is significant noise experienced throughout the impact surface analyzed in the experiments performed. For this report, a larger strain radius is used to average out the noise and provide smoother strain fields. An example of strain analysis performed using a small compared to large strain radius for an experimental trial is shown in Figure 3. The strain calculation process yields data and visual gradient images of axial, shear, and principal strains. Saving the data for multiple trials allows for averaging to find mean and standard deviation for the strain values.

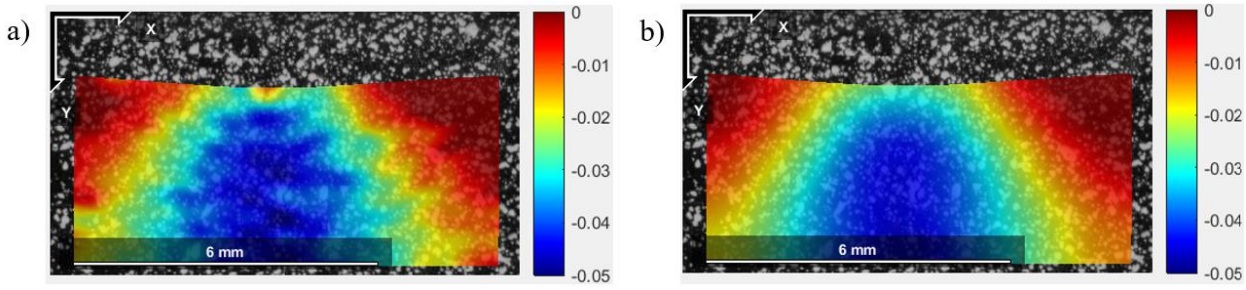

Figure 3 – DIC strain results using a a) small strain radius of 15 pixels (0.1083 mm) compared to a b) large strain radius of 40 pixels (0.2888 mm).

CHAPTER 2: EXPERIMENTAL PROTOCOL

2.1 Camera Setup

A camera (Kron Technologies Chronos 1.4 monochrome) is used to capture the displacement of the speckles on the polymer surface during impact. A microscope lens (Navitar 12x Zoom Lens system with 1-50487 body tube, Navitar, Inc.) is added to view in detail the contact area between the granules and polymer. The impact is rapid and a high frame rate is used to capture a frame at max compression. The camera is equipped with different frame rate and resolution combinations. In an ideal scenario, it is optimal to record at a high frame rate using a large resolution to capture as many images as possible during compression over a large area. However, there are tradeoffs between frame rate and resolution. Using a higher framerate not only darkens the image, but also reduces the resolution of the recording. On the other hand, the camera limits using a large resolution to a lower frame rate. It was found that using a resolution of 1280x720 at 1519 fps (FPS) allowed us to capture one clear frame between the downward and upwards movement of the speckles. This singular frame is considered the max compression of the polymer during the impact.

The images during the compression stage are blurry and not able to be analyzed by ncorr so we were unable to demonstrate the change in strain over the compression period for different time intervals. The max compression image can sometimes be clearer on some trials than others mainly when rotating pucks around. The analog gain is tuned to 18dB (8x) to decrease the read noise and increase the quality of the recordings. Increasing the analog gain makes it possible to measure smaller differences in light intensity from the reflective white speckles and lighting. There is no digital gain added. The camera settings remain constant for all experiments. The

camera is set on a tripod which remains stationary during experiments. However, the height changes depending on the granular media combination.

2.2 Granular Media

Wooden, cylindrical pucks of varying sizes are used to model granular media. The pucks were included with the baseline toy further discussed in section 2.3. The material properties of the pucks are unknown, as the wood used is not provided by the manufacturer. As the elastic modulus of wood is significantly greater than the polymer being evaluated, it is not critical to report the specific material properties of the wooden pucks. The red (R) is the smallest diameter, yellow (Y) is the next largest diameter, and blue (B) is the largest diameter. Figure 4 is a representation of the puck sizes relative to each other. Table 1 shows the pucks with their respective dimensions and length of granular media row in contact with the polymer. The length of granular media row is the total length over which the pucks are on top of the polymer. It is calculated for every combination as,

$$L = n * d$$

Where L is the length of granular media row in contact with polymer, n is the number of granules used, and d is the diameter of an individual granule. All the pucks have the same thickness and are equal to the thickness of the polymer.

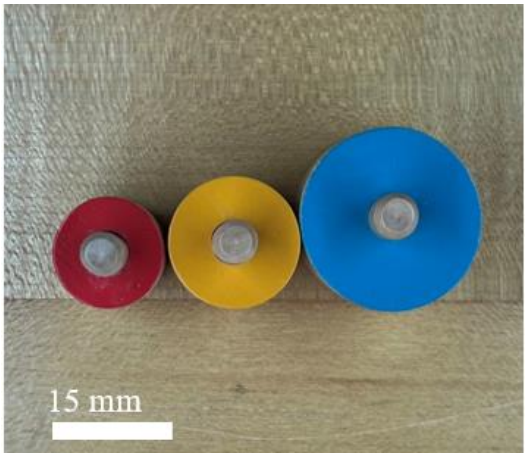

Figure 4 – Snapshot of Pucks Used.

Combinations of granular media in rows are experimented to determine possible relationships between puck size and impact strain experienced by the polymer. Figure 5 depicts the four combinations of granular media arrangements used. For simplicity's sake, the combinations have been abbreviated throughout the paper where each of the letters stands for the granule sizes used in that row. For instance, the RRR scenario contains a row of red pucks only in the bottom, middle, and top layers. The bottom layer is the layer in contact with the polymer, and the top layer is the layer that receives the impact from the spring-block system. Figure 5a contains the YYY combination. Figure 5b contains the RRR combination. Figure 5c contains the YRY combination. Figure 5d contains the BBB combination. For all combinations, the pucks making up the bottom row are labeled. The RRR, RYR, and RRR combinations have a row of 4 pucks placed between two rows of 5 pucks; this number of pucks is used to resemble the computer model from Vakakis *et al*. [5]. To maintain consistency between combinations, the same number of granules is used. The BBB combination is an exception, as contains a row of 2 pucks placed between 3 pucks in the bottom and top rows. The large size of the pucks would not allow proper capturing of wave propagation through the polymer as the outer pucks are too close

to the inner wall of the apparatus if 5 pucks are used in the bottom layer. The results from the BBB combination are discussed as an extension of the experimental work, done but are not confirmed to yield the same results as if using fourteen pucks like the other combinations.

Table 1 - Granule and Granular Media Dimensions.

Puck	**Diameter [mm]**	**Thickness [mm]**	**Length Of Granular Media Row (L) [mm]**
Red	14.5	10	72.5
Yellow	16.7	10	83.5
Blue	23.7	10	71.1

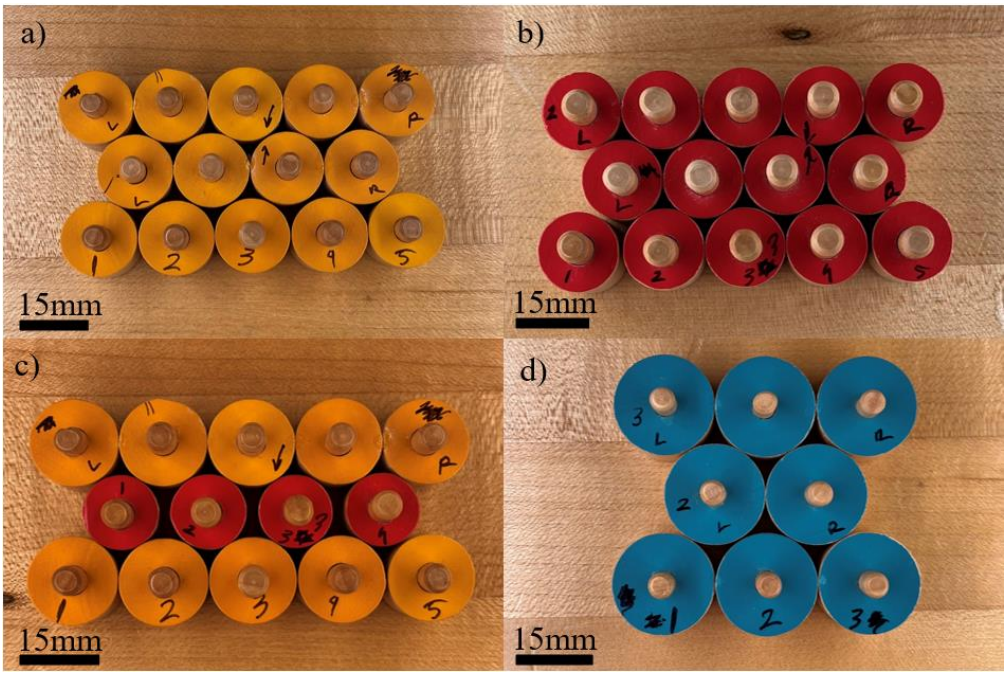

Figure 5- Granular Media Combinations with Pucks Labeled.

Choosing an odd number of pucks to be in contact with the polymer allows for the ability to record and analyze the granular-solid interface for the middle puck, left most puck, and right

most puck and observe possible symmetry effects. To prevent the pucks from moving directly after impact, the top row pucks are lined up and glued together. The middle and bottom rows are not glued but free to rotate as there is a holder keeping the granular media in place following impact. The diameter of the pucks can vary slightly from puck to puck. Pucks in contact with the polymer are moved around between trials to reduce error from to the varying diameters within each puck size. There are three puck rotations for each granular media combination. Within each rotation, five trials are conducted for the camera focused on the center puck, left most puck, and right most puck. That is, there are 15 total trials conducted per puck rotation, and 45 per combination. Since there are 4 granular media combinations, a total of 180 trials are performed. The order of the puck rotations for YRY, YYY, and RRR trials are labeled on Table 2. Only the pucks in contact with the polymer are moved around; the top row of granular media is glued together in a straight line. Therefore, there is a possibility that the diameter differences in the pucks within the top row results in certain pucks being impacted slightly before the others. While the difference in impact time is very minimal, it presents a source of error that could propagate through the rest of the granular media.

Table 2 – Puck Rotation Combinations.

Puck Rotation Combination	YYY, RRR, YRY Puck Order	BBB Puck Order
1	1 2 3 4 5	1 2 3
2	5 2 3 4 1	3 2 1
3	3 4 5 1 2	2 3 1

During and after impact, the pucks in the bottom and middle rows are free to rotate. This serves as an added source of variability between trails of the same puck rotation. The

computational model ran by Vakakis *et al.* accounts for rotational frictional effects, which are experienced by the bottom and middle layer pucks in the experiments run through this apparatus. However, as previously mentioned, gluing the top row could result in the pucks in the row acting as one whole rigid surface. This results in no frictional effects within the top row, which could propagate through the granular media and reduce the rotation of the middle and bottom pucks.

2.3 Fabrication of Impact Force Apparatus

Figure 6 presents a view of a toy consisting of a spring-block system that was used as the baseline for the experimental apparatus. The toy consists of a rod attached to a block with a stopper at the end. The block is contained within a frame, and the rod is able to go through a hole opening on the top side of the frame. There is a spring around the rod held in place by the block and the frame. There is also a stopper attached to the end of the rod on the outside of the frame which facilitates the pulling of the block in the negative y direction, thus compressing the spring. When released, the spring-block system travels in the positive y direction. The impact force applied to the granular media originates from compressing the spring-block system by a distance of 1cm. The coordinate system of the apparatus is labeled in 2D in Figure 6 but can be better seen in 3D in Figure 11, where the z direction points out and is positive towards the camera. Motion of the system is restricted in the z and x directions by the frame of the toy. Therefore, the movement of the block and spring is 1D in the y direction.

Large tolerances within the toy's frame result in areas of wiggle in the z and x directions and are possible sources of error during trial testing. Wiggle in the z direction originates from the difference between the diameter of the rod that connects the block to the release point and the hole in the frame through which the rod goes through. The distance between the inner walls is less than the length of the block; as such, the block can translate in the x direction and rotate a

few degrees depending on how the spring is released. A 3D print is implemented to tighten the block between the print and back wall of the toy and reduce wiggle in the z direction while allowing the block to freely slide along the y direction. Fabrication of a future apparatus would benefit from tight tolerances between the spring-block system and the frame holding the system in place.

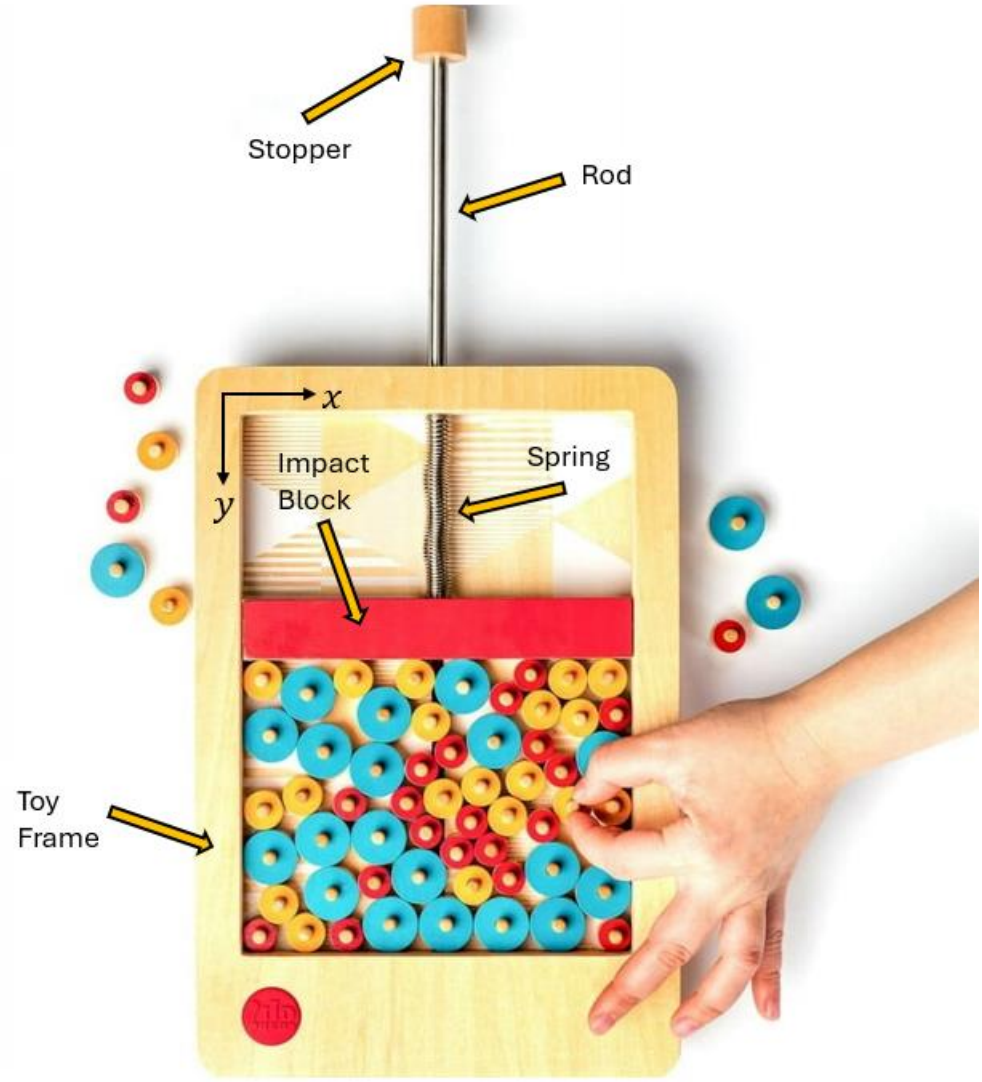

Figure 6 - Marbles OhSnap! toy used as apparatus baseline (image adapted from ref. [33]) .

The toy is unable to be stationary in vertical position by itself. A stand is fabricated to hold the toy in an upright position for testing. The stand is made from wood, screws, and metal L shape joints. The final apparatus is perfectly horizontal in the x and z directions and vertical in the y direction. As the length of the polymer matches the inner side of the walls, no displacement of the polymer as a whole occurs in the x direction during testing. To prevent the polymer from displacing towards the camera between trials, a holder was designed in SolidWorks and 3D printed using PLA filament and 10% infill. When installed, the polymer holder has 0.5-1mm of tolerance between the holder itself and the polymer to prevent the holder from compressing the polymer and decreasing the wave propagation from the impact. After impact, the whole polymer slightly displaces axially in the direction of the impact. However, the displacement is negligible as interest is only to capture maximum compression during initial impact.

To prevent the granular media from displacing sideways or towards the camera during testing, granular media holders are designed and 3D printed for each unique combination in the same way as the polymer holder. The holder prevents the pucks from translating in the x direction by constraining the bottom pucks and allows the granular media to be in the same location relative to the polymer speckles for each trial. The granules displace in the y direction after the initial impact. However, the granular media holder is high enough to account for the displacement and allows the pucks to slide down to the original position after impact. The top row of the granular media keeps the middle pucks from moving out of their location.

The impact force from a spring block system varies by spring length at impact regardless of a constant initial compression length. This is visually represented on a diagram in Figure 7. where k is the spring constant, $L_{c,i}$ is the spring compression length at impact and, L_0 is the uncompressed spring length. The diagram represents two separate granular media combinations

during testing. The combinations are tested using the same apparatus and have the same frame, spring, and impact block. The springs are initially compressed by the same distance. When released, the block impacts the YYY granular media combination with a force F_{YYY}. Similarly, the block impacts the RRR granular media combination with a force F_{RRR}. The YYY granular media combination is impacted first, as the height of the combined rows is greater. At this time, the springs for both scenarios are at a length of $L_{c,i}$; however, the block is a distance of h from impacting the top row of the RRR granular media combination while it has already impacted the top row of the YYY combination. When the block impacts the RRR combination, the spring compression length will be different compared to the spring compression length at impact for the YYY combination. The formula for spring force is:

$$F = k * x$$

where F is the force, k is the spring constant, and x is the length of the spring. At impact, the spring length varies depending on the combination due to the height difference h between the top layers of granular media. Therefore, $F_{RRR} \neq F_{YYY}$ and the different combinations of granular media experience a different impact force.

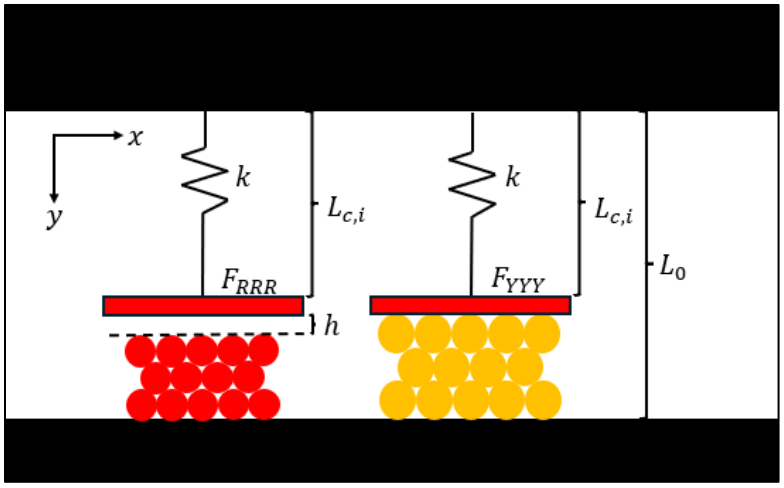

Figure 7 - Diagram of spring compression length difference at impact between combinations.

To normalize impact force for all granular media combinations, blocks of different heights are designed and 3D printed using similar methods above. The blocks are placed under the polymer and raise the polymer-granular media combination so that the top row of all granular media combinations are at the same height, or distance from the block during initial spring compression. A holder is implemented to secure the blocks in place similarly to the polymer holder. Figure 8 highlights the apparatus without the holders for the RRR combination. The granular media are lined up so that the center puck of the top and bottom rows are aligned with the rod and spring. The frame holds the toy in place during testing and is clamped during testing to prevent displacement during impact (not shown in the figure). The height blocks printed are slightly thicker than the polymer and the same length as the inner frame of the toy. Figure 9 highlights the apparatus with the spring compression block, granular media holder, polymer holder, and height block holder for the RRR combination. The holders are screwed into the wooden frame of the apparatus in locations depending on the height block used for the tested combination. The granular media holder is screwed in place so that it does not touch the polymer.

When interchanging the puck order of the bottom row, the granular media holder is removed and then reinstalled.

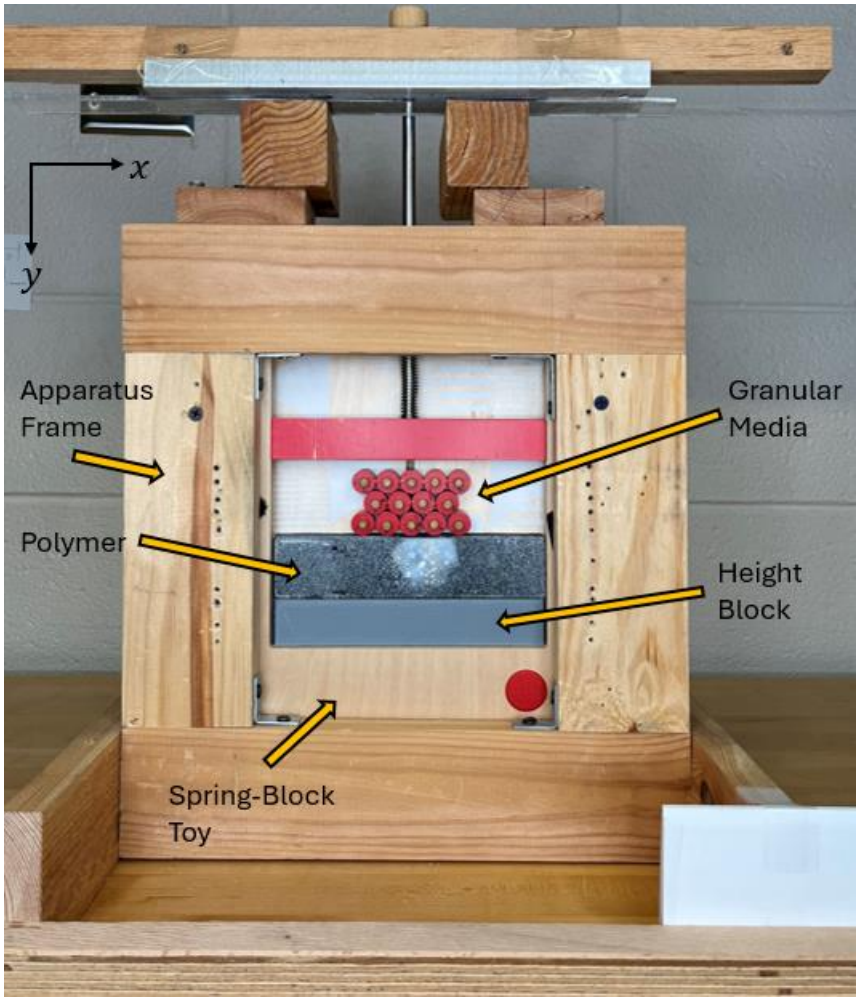

Figure 8 – Apparatus modified for RRR combination without granular media holder to show pucks, polymer, and added height block.

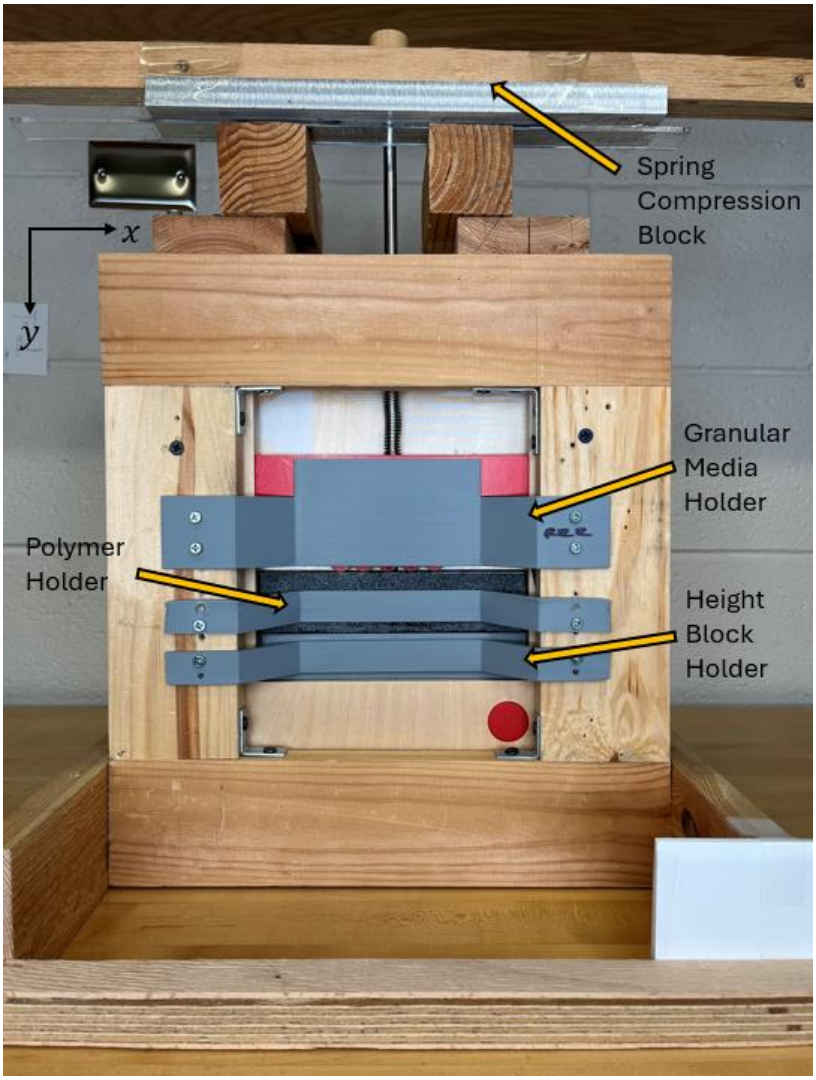

Figure 9 - Apparatus modified for RRR combination with holders during testing.

2.4 Fabrication of Impact Surface Polymer

The impact surface (referred to as polymer) is selected to be made from PDMS due to its flexibility and ease of production compared to other materials [33]. Elastomers such as PDMS are flexible and able to restore the original shape after stress is applied. The elastic properties of PDMS are key for this research as DIC depends on being able to clearly determine surface displacements to find the strains. The ability of the polymer to restore itself to the original shape allows for trials to be conducted using the same polymer without having the material properties change. The low cost and rapid prototyping ability associated with PDMS allows for simple production of multiple polymers provided there is damage to one during trial testing [34].

The polymer fabrication process is illustrated in Figure 10. The polymer block is fabricated using Sylgard 184 PDMS, black paint, and patterned with spray paint. Fabrication begins by mixing Sylgard 184 parts A and B using a 10:1 mass ratio. It takes about 50g of part A and 5 of part B to have more than enough mixture to make a block. After mixing for 10 minutes, Createx opaque black airbrush paint is added at a mass ratio of 1:150 (paint to mixture) and mixed for an additional 5 minutes. The dark gray mixture is then degassed in a vacuum at room temperature for 5 minutes at 200 mbar and then 25 minutes at 100 mbar. The degassed mixture is poured in a mold up to the brim and excess wiped off. The mold is placed in an oven and cured at 75℃ for 7 hours. After the time is reached, the molds are taken out and allowed to cool for several hours before the solid roller is extracted by using an x-acto knife to separate the edges of the polymer from the mold before carefully peeling it out.

The polymer is cleaned using water and soap before an x-acto knife is used to carefully cut away excess PDMS that sticks out of the edges. Two polymers are produced in this fashion and then glued together. The “glue” is made using the exact same mixture ratios of PDMS part A

and B using 10 grams of part A. The mixture is degassed with the same method and applied between the two polymers. After applying pressure to the joined polymers for an hour or so, the combined polymer is placed in the oven at a temperature of 75℃ to cure for 1 hour. Extra mixture spilling from the sides is wiped off prior to the curing process. Once the time is reached, the polymer is taken out and let to cool off for a couple of hours. A small meniscus commonly forms on the side of the polymer that is cured not in contact with the mold. Although it does not affect the joining of the polymers, it is carefully sanded off from the final polymer to create a flat surface that will be in contact with the wooden apparatus. The elasticity of Sylgard 184 can be tuned depending on the ratio of base to curing agent A:B. A 10:1 base-to-curing agent is recommended by the manufacturer and once cured yields a young's modulus range of 1.3-2.97 and a poisons ratio of 0.495 [35]. The properties of the polymer are seen on Table 3.

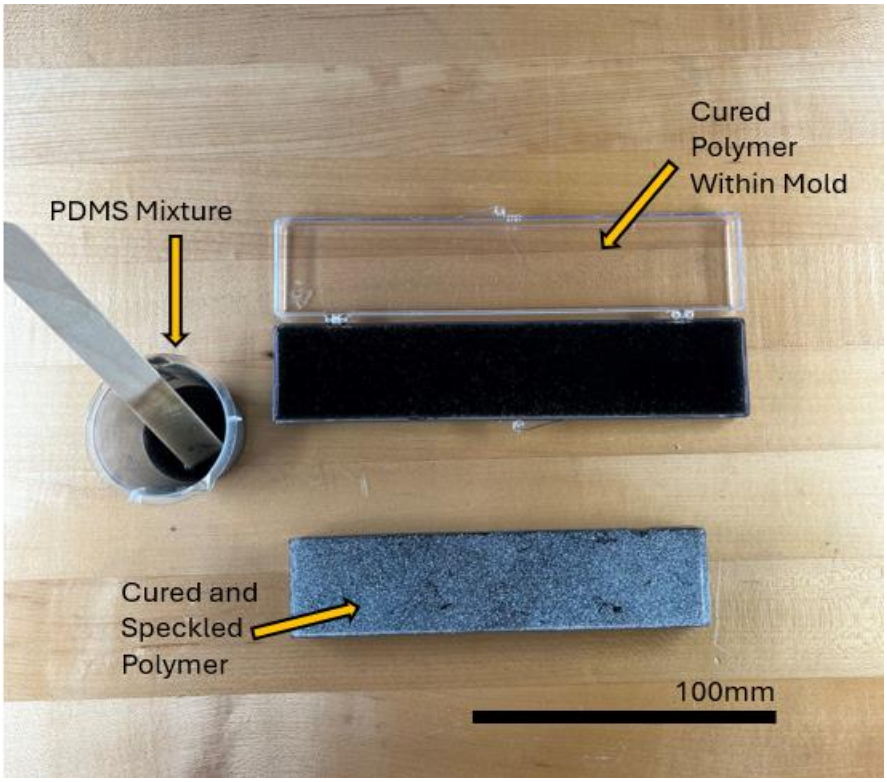

Figure 10 - An optical image of the process followed to fabricate the polymer.

Table 3 – Material Properties of PDMS

	1 (PDMS Polymer Block)
$\boldsymbol{E}$	1.85 MPa
$\boldsymbol{v}$	0.495

2.5 Patterning of Polymer

The side of the polymer cured in contact with the mold is cleaned and speckled using a pattern of random speckles with an average diameter of 0.1mm. Reflective white spray paint is used to spray a fine mist from around 2 feet away using a side-to-side motion to apply the speckles on the polymer surface. Speckles must be evenly distributed around the polymer surface and close to the edges. To prevent the speckles from smearing during handling and experiment installation, the polymer is cured at 75℃ for 1 hour after speckles are applied. Once the speckles are cured, the back side of the polymer is spray painted black and cured at 75℃ for 1 hour. Painting the back of the polymer black increases the visibility of the reflective white speckles and leads to better DIC analysis results.

2.6 Experimental Setup

The experimental setup consists of the impact apparatus, lighting, clamps, a height block to compress the spring, a straight wood stick, and a camera equipped with a magnifying lens. Figure 11 shows the labeled experimental setup. Capturing movement with a high frame rate results in shorter exposure time and darkened images. A ring light with two other auxiliary light sticks angled at 45 degrees relative to the polymer are used to illuminate the speckles during testing. A holder for the two auxiliary lights is modeled using SolidWorks and 3D printed using PLA at 10% infill. During testing, the camera remains stationary while the setup is moved

manually along the x direction depending on the location of the polymer being recorded. The ability to maintain the camera stationary allows for the polymer to be recorded at a constant height between trials for each granular media combination. If the camera is moved, the unevenness of the floor tilts the camera and requires readjusting. The same speckle pattern and area is recorded for the different puck rotations within the same granular media combination. However, the height of the camera is adjusted depending on the combinations; this is due to the addition of the height block to normalize the impact height of all combinations (adding the height block raises the polymer). Furthermore, the speckle pattern area used changed slightly between combinations as the length of granular media row in contact with the polymer changed changes depending on the pucks being used (see section 2.2).

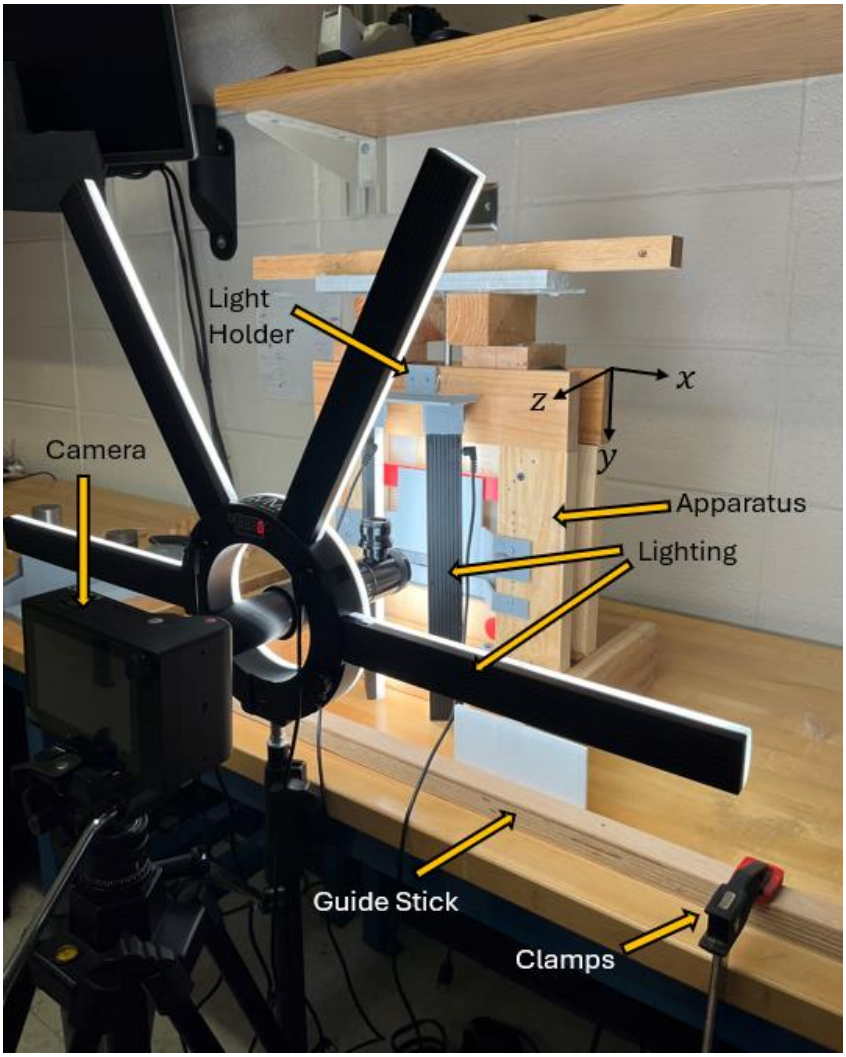

Figure 11 - Experimental Setup.

A table length, straight, wooden stick is clamped in place to aid the apparatus movement between different combination recordings. The stick is clamped so that it is parallel to the camera lens, and at a distance that focuses the camera resolution on the speckles. This way, the apparatus is free to slide along the length of the stick, and when bought towards the camera, will focus when it is up against the stick. Clamps are used to set the apparatus in place and prevent movement from the impact between trials. A height block is used to compress the spring-block system by the same displacement every trial. A compression length of 1 cm is used. The stopper

attached to the rod allows the height block stay in place and keep the spring compressed until removed. During testing, the block is manually pulled in the positive z direction (towards the camera) using two hands, thus releasing the spring from a constant height every trial. To reset the setup before each trial, the stopper is lifted and the height block placed between the apparatus and stopper. The apparatus, stopper, and height block are all horizontal, and there is no height gradient while pulling the height block.

Granular media holders and the height blocks that raise the polymer are manually removed and changed when changing granular media combinations. The changing of these occurs with the setup in a horizontal position to prevent damage to the speckled polymer from the pucks falling out when removing the granular media holder. Although the height blocks do not change when rearranging pucks for testing within the same granular media combination, the granular media holder is removed to rearrange the pucks and check for damages. The steps for trail testing are as follows:

1. Verify camera and lights are plugged in.
2. Turn on lights and camera.
3. Verify camera settings are correct (refer to camera settings section).
4. Verify camera lens is parallel to wood piece and that wood piece is securely clamped in place.
5. Move apparatus to desired location.
6. Clamp apparatus in place.
7. Raise spring-block system.
8. Use height block to compress spring.
9. Hit record on camera.

10. Pull height block.
11. Stop recording on camera.
12. Trim initial impact and save video clip.

2.7 DIC Analysis Parameters

There are several steps within ncorr and parameters that must be adjusted after selecting the reference and current images. The reference image used is the speckled area of the polymer before compression, while the current image used is max compression area of the polymer. A region of interest (ROI) is defined over which the displacements and strains will be calculated. There is a “buffer” area between the edges of the region of interest and the total image sides to avoid errors from trying to analyze speckles that have displaced completely out of the frame (shown in Figure 12). After selecting the ROI, the DIC parameters are selected. The subset radius is set at 29, the subset spacing is set at 2, the max iteration no. for an initial guess is set at 50, the multithreading option is selected based on the number of computational cores available, high strain analysis is turned off, and subset truncation is turned off. There is a tradeoff between the subset radius and computational speed. A larger subset radius allows for faster computation, but the results can be less accurate. Likewise, a smaller subset spacing creates more subsets and leads to more accurate results but takes a longer computation time. The number of seeds for DIC analysis is directly proportional to the number of cores used (ie. 4 cores = 4 seeds) and manually selected within the ROI. The seeds are spaced out and preferably selected as speckles that are easily distinguishable between the undeformed and deformed images. Figure 13 shows an example of seed selection; ncorr can match the speckles between the undeformed and deformed images if the deformed image is not too blurry. However, the less blurry the deformed image, the better the results from DIC.

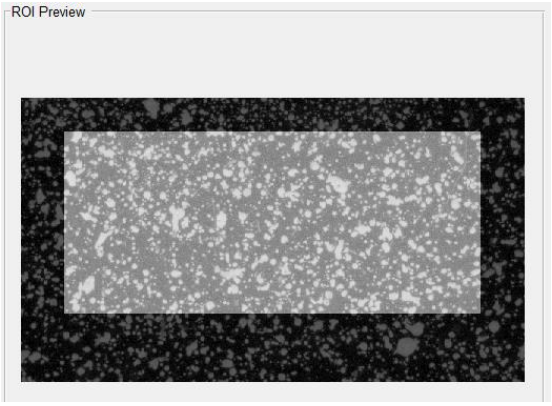

Figure 12 – A selected region of interest (depicted in white) over the reference image.

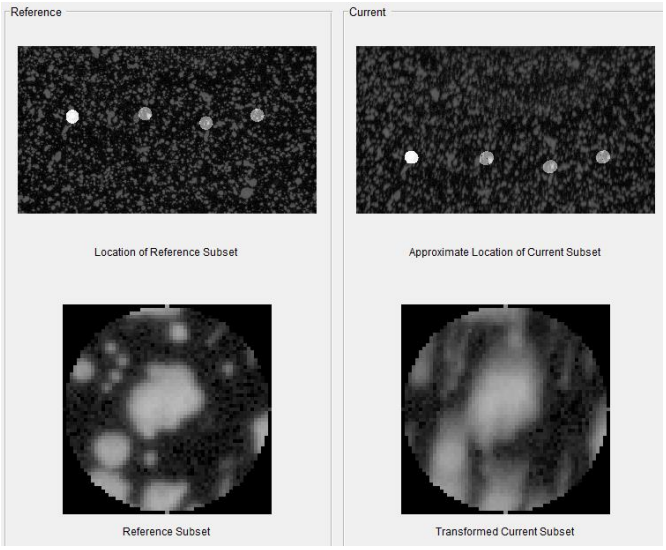

Figure 13 - A comparison of the selected seed locations in the reference and deformed images.

Once the image undergoes the DIC analysis, the displacements can be formatted. There is an option to convert units which was done for the figures in the results section from pixels to mm. The lens distortion options are turned off, and the zoom/pan options remain untouched. Finally, the strain parameters are selected. The strain radius has a range of 0 to 50 pixels and is set at 40 pixels (refer to section 1.4). As previously discussed, changing the strain radius can

allow for localized strain effects to be observed or create smooth visuals. There is significant noise during impact, so a larger strain radius is chosen. Subset truncation is turned off and the zoon/pan options remain untouched. A preview of the strain field calculated over a certain displacement field is shown in Figure 14. A small deviation between the subset strains (blue points) to the plane is preferred as it yields smoother results. Once finalized, the displacement and strain plots are available to see with a Green-Lagrangian view on the undeformed image and a Eulerian-Almansi view on the deformed surface. Axes, a scalebar, and bounds are defined.

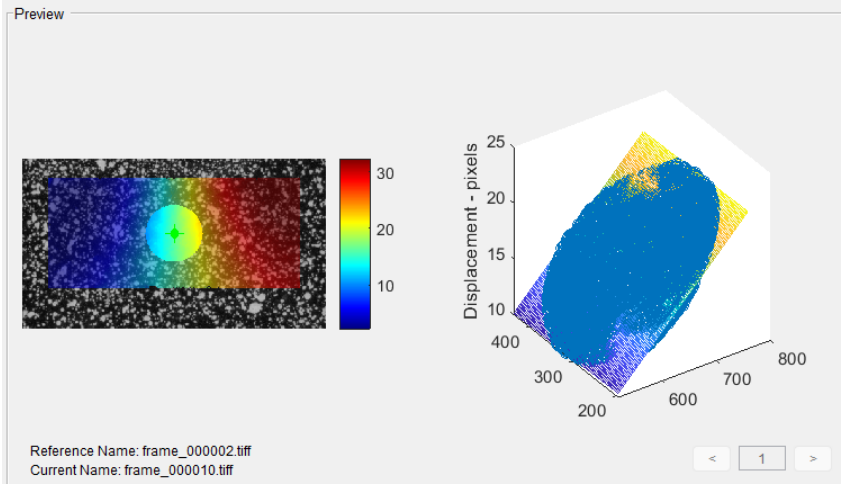

Figure 14 – Preview of strain field with selected strain radius.

CHAPTER 3: MEASUREMENTS GAINED FROM APPARATUS

3.1 DIC Strain Fields

Strain fields of the polymer during max compression for the different granular media combinations are presented in this section. The data used by ncorr is an undeformed image and a and an image at max compression. The frames between the undeformed image and the max compression image were too blurry to be analyzed by ncorr. For this reason, the rate of deformation was unable to be calculated. Contact behavior of a rigid granule with an elastic

boundary is complex and results vary between trials. The strain fields depicted are an average of the strain fields calculated by ncorr for every individual trial. It can be noted that due to the averaging of the leftmost and rightmost granules for the side strain fields, there is a rectangular area on the outer sides of the strain field that is close to zero value. This occurs during the averaging process as the displacement of the speckles is skewed on the sides during max compression depending on the side being recorded. As previously mentioned (refer to section 2.2), the BBB combination only had three contact points compared to five for the rest of the combinations. Therefore, the results are not representative of a scenario where 5 blue contact granules are used. The results from the BBB combination are included for future reference but are not discussed in this paper.

Figure 15 presents the normal strains in the y direction (ε_{yy}). Figures 15(a,c,e,g) correspond to the area under the center granule. Figures 15(b,d,f,h) correspond to the area under the side granules. For the side granule figures, the strain fields for the right most granule and the left most granule are averaged together. The min and max absolute values are labeled in each figure. Figure 15(a-b) display the ε_{yy} field for the RRR combination. The outer most side granules experience more strain than the center granule. Figure 15(c-d) display the ε_{yy} field for the YRY combination. The outer most side granules experience slightly more strain than the center granule. Figure 15(e-f) display the ε_{yy} field for the YYY combination. The center granule experiences significantly more strain than the side granules. Figure 15(g-h) display the ε_{yy} field for the BBB combination. The center granule experiences significantly more strain than the side granules. For all combinations, the strain appears to be concentrated in the center (under the point of contact) and disperses outwards. The strain distribution follows a conical shape downwards.

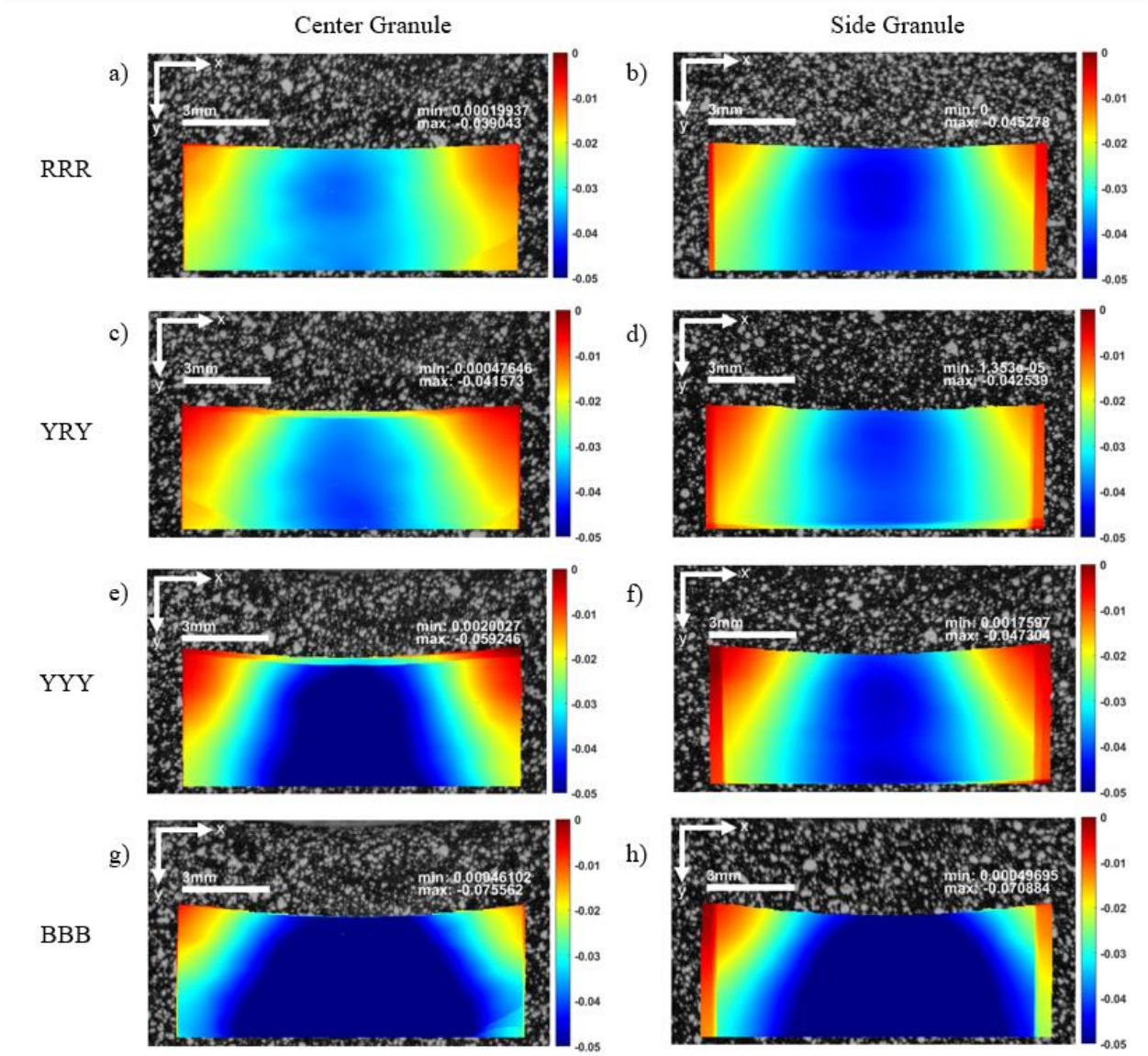

Figure 15 - Strain fields in the normal y direction (ε_{yy}) of the polymer at max compression for the granular media combinations tested. (a), (c), (e), (g) - strain fields of the area under the center granule. (b), (d), (f), (h) – strain fields of the averaged area under the side granules.

The area under the center granule experiences a max strain of -0.0390, -0.0415, and -0.0592 for the RRR, YRY, and YYY combinations respectively. The area under the side granule experiences a max strain of -0.0452, -0.0425, -0.0473 for the RRR, YRY, and YYY combinations

respectively. There is less strain being experienced by the center granule for the RRR combination (Figure 15a) than the YRY combination (Figure 15c), but there is less strain experienced on the side granule for the YRY combination (Figure 15d) compared to the RRR combination (Figure 15b). The values between these two combinations are small, but both combinations experience significantly less strain under both areas than the YYY combination. Although the YYY and YRY combinations have the same granules in contact with the polymer, the addition of smaller (red) granules in between the layer of yellow granules results in a decrease in strain under both the side and center granules.

Figure 16 presents the normal strains in the x direction (ε_{xx}). Figures 16(a,c,e,g) correspond to the area under the center granule. Figures 16(b,d,f,h) correspond to the area under the side granules. For the side granule figures, the strain fields for the right most granule and the left most granule are averaged together. The min and max absolute values are labeled in each figure. Figure 16(a-b) display the ε_{xx} field for the RRR combination. The outer most side granules experience more strain than the center granule. Figure 16(c-d) display the ε_{xx} field for the YRY combination. The center granule experiences significantly more strain than the side granules. Figure 16(e-f) display the ε_{xx} field for the YYY combination. The center granule experiences significantly more strain than the side granules. Figure 16(g-h) display the ε_{xx} field for the BBB combination. The center granule experiences significantly more strain than the side granules. For all combinations, the strain appears to be concentrated in the center (under the point of contact) and disperses outwards. The strain distribution follows a semicircular shape downwards.

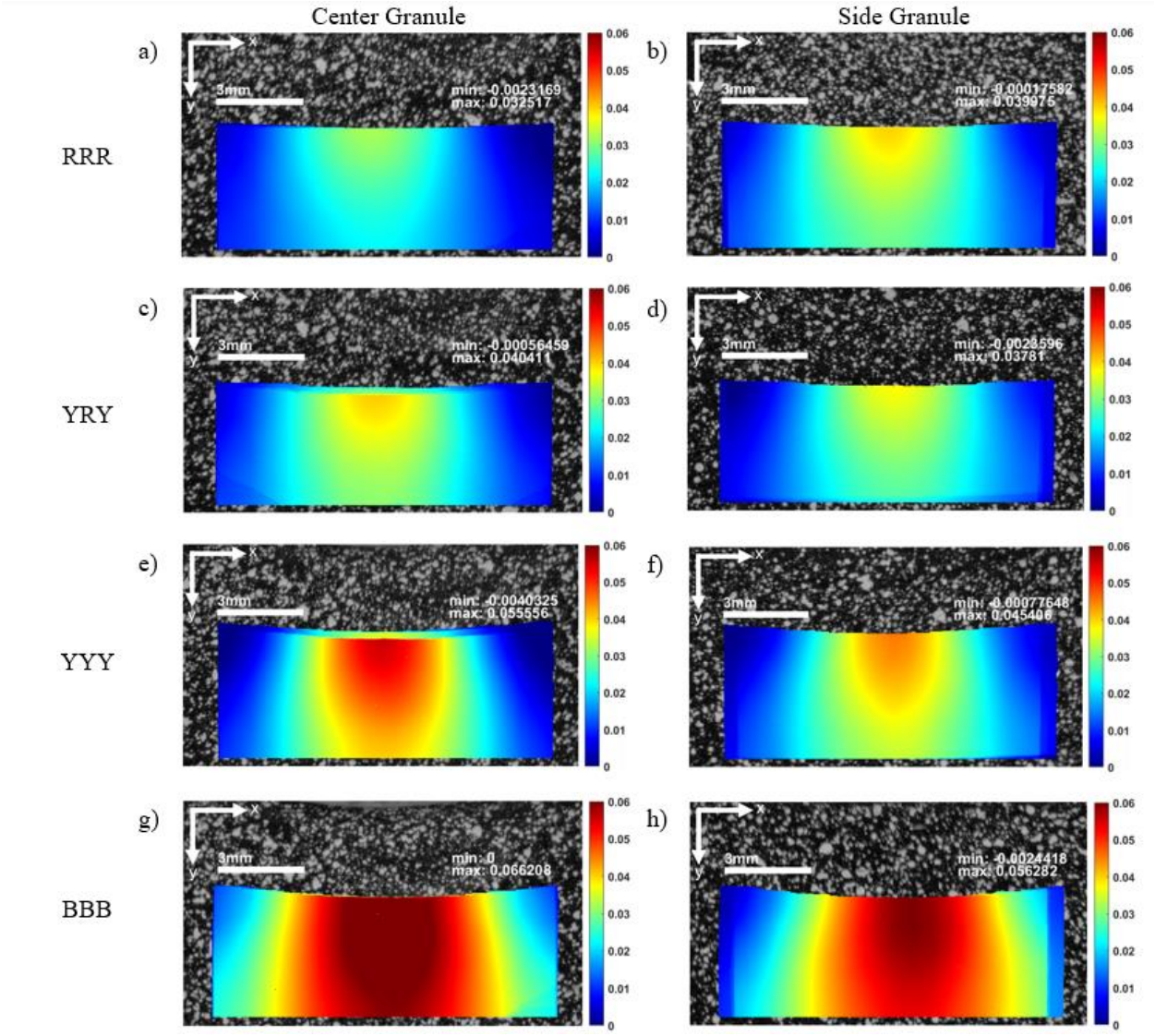

Figure 16 - Strain fields in the normal x direction (ε_{xx}) of the polymer at max compression for the granular media combinations tested. (a), (c), (e), (g) - strain fields of the area under the center granule. (b), (d), (f), (h) – strain fields of the averaged area under the side granules.

The area under the center granule experiences a max strain of 0.0325, 0.0404, and 0.0555 for the RRR, YRY, and YYY combinations respectively. The area under the side granule experiences a max strain of 0.0399, 0.0378, 0.0454 for the RRR, YRY, and YYY combinations

respectively. The max strain experienced as well as the strain distribution for the area under the center granule increases in the order RRR, YRY, and YYY as seen on Figure 16(a,c,e). For the area under the side granules, the max strain values and distribution is similar for the RRR and YRY combinations, but significantly increases in the YYY combination. Like ε_{yy}, ε_{xx} is reduced in the areas under the center and side granules when the middle row is replaced from yellow pucks to red pucks between the YYY and YRY combinations.

Figure 17 presents the shear strains in the x-y direction (ε_{xy}). Figures 17(a,c,e,g) correspond to the area under the center granule. Figures 17(b,d,f,h) correspond to the area under the side granules. For the side granule figures, the strain fields for the right most granule and the left most granule are averaged together. The min and max absolute values are labeled in each figure. Figure 17(a-b) display the ε_{xy} strain for the RRR combination. The outer most side granules experience more positive and negative shear strain than the center granule. Figure 17(c-d) display the ε_{xy} strain for the YRY combination. The outer most side granules experience more positive and negative shear strain than the center granule Figure 17(e-f) display the ε_{xy} strain for the YYY combination. The center granule experiences significantly more positive and negative shear strain than the side granules. Figure 17(g-h) display the ε_{xy} strain for the BBB combination. The center granule experiences significantly more positive and negative shear strain than the side granules. For all combinations, the strain appears to be concentrated in the in the locations furthest from the point of contact along the x axis. There is a region of no shear along the y axis directly under the point of contact of the granule; this region is noticeable in green and is a transition between the positive and negative shear strain. A symmetry effect can be seen along across this axis where there is negative ε_{xy} on the right side and positive ε_{xy} on the

left side. Furthermore, the shear strain appears to be more localized in the area closer to the granule and dissipates as the region gets further from the contact point along the y axis.

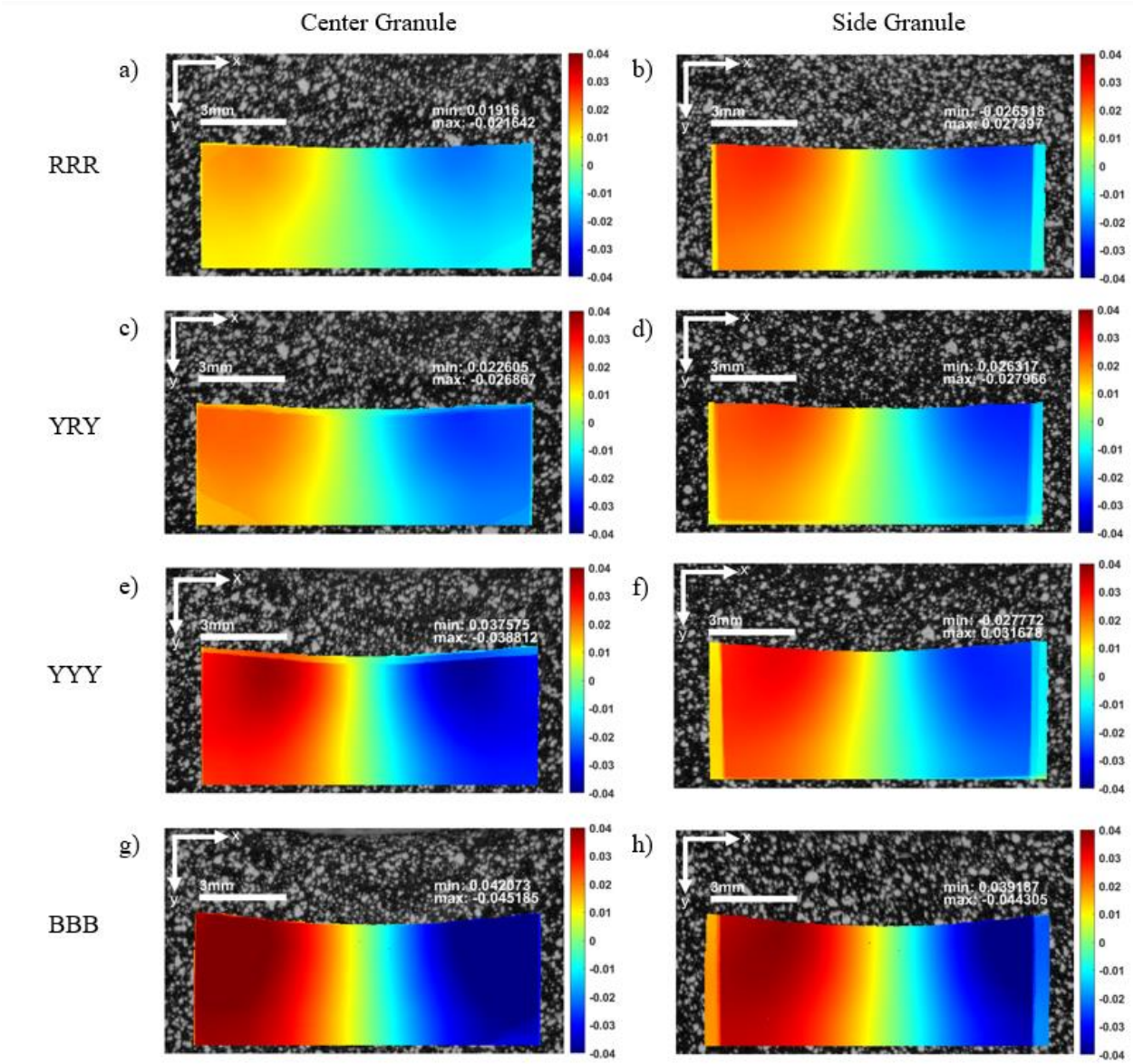

Figure 17 – Shear strain fields (ε_{xy}) of the polymer at max compression for the granular media combinations tested. (a), (c), (e), (g) - strain fields of the area under the center granule. (b), (d), (f), (h) – strain fields of the averaged area under the side granules.

The values and fields under the center granule for the RRR (Figure 17a) and the YRY (Figure 17c) combinations are similar. The same relationship is observed for the fields under the side granule for the RRR (Figure 17b) and the YRY (Figure 17d) combinations. The fields for the center and side granules for the YYY (Figure 17e and Figure 17f respectively) are of greater magnitude than the RRR and YRY fields. The addition of the red row has a significant effect on the shear strain experienced by the polymer despite having the same yellow row in contact between the YRY and YYY combinations.

The standard deviations between trials for the types of strains are calculated to show the testing repeatability and accuracy of the apparatus. An example of standard deviation fields for the area under the center granule in the RRR combination is shown in Figure A.1 within Appendix A. The remaining standard derivation fields are not displayed as they follow the same trend and value ranges. The standard deviations are close to zero within the region of interest despite the polymer compressing a slightly different amount between trials.

3.2 Energy-like Quantity Fields

An energy-like quantity (E) experienced by the polymer is calculated and plotted in fields to visualize the overall impact of the different strains. The E fields at max compression for every combination are presented in this section. A relationship between strain and the energy-like quantity is obtained by squaring the strain components individually and then summing them up:

$$E = \varepsilon_{yy}^2 + \varepsilon_{xx}^2 + \varepsilon_{xy}^2 \tag{14}$$

where E is the energy-like quantity and ε_{yy}, ε_{xx}, and ε_{xy} are the strains previously calculated from ncorr. The strain fields depicted are an average of the strain fields calculated by ncorr for every individual trial. Only the normal strains in the x direction, y direction, and xy shear are

taken into account due to the 2D limitations from ncorr. For this paper, the 2D coordinates are limited to the x and y directions. However, it is important to consider the normal strain in the z direction is not zero due to the Poisson effect. This strain was unable to be measured by ncorr but could be an extension of future work. The same rectangular area on the outer sides of the E fields is created during the averaging process as the summed strains contain these outer borders (see section 3.1). As previously mentioned, the E results from the BBB combination are included for future reference but are not discussed in this paper.

Figure 18 presents the E fields for the different granular media combinations. Figures 18(a,c,e,g) correspond to the area under the center granule. Figures 18(b,d,f,h) correspond to the area under the side granules. For the side granule figures, the E fields for the right most granule and the left most granule are averaged together. The min and max absolute values are labeled in each figure. Figure 18(a-b) display the E field for the RRR combination. The outer most side granules experience more E than the center granule. Figure 18(c-d) display the E field for the YRY combination. The outermost side granules experience slightly more E than the center granule. Figure 18(e-f) display the E field for the YYY combination. The center granule experiences significantly more E than the side granules. Figure 18(g-h) display the E field for the BBB combination. The center granule experiences significantly more E than the side granules. For all combinations, the E appears to be concentrated in the center (under the point of contact) and disperses outwards. Due to the addition of all the strains, there is not a consistent shape for the E fields. The fields for the RRR combination in Figure 18(a-b) appear more concentrated as a semicircle compared to the fields for the YYY combination are more concentrated in a conical shape as seen on Figure 18(e-f).

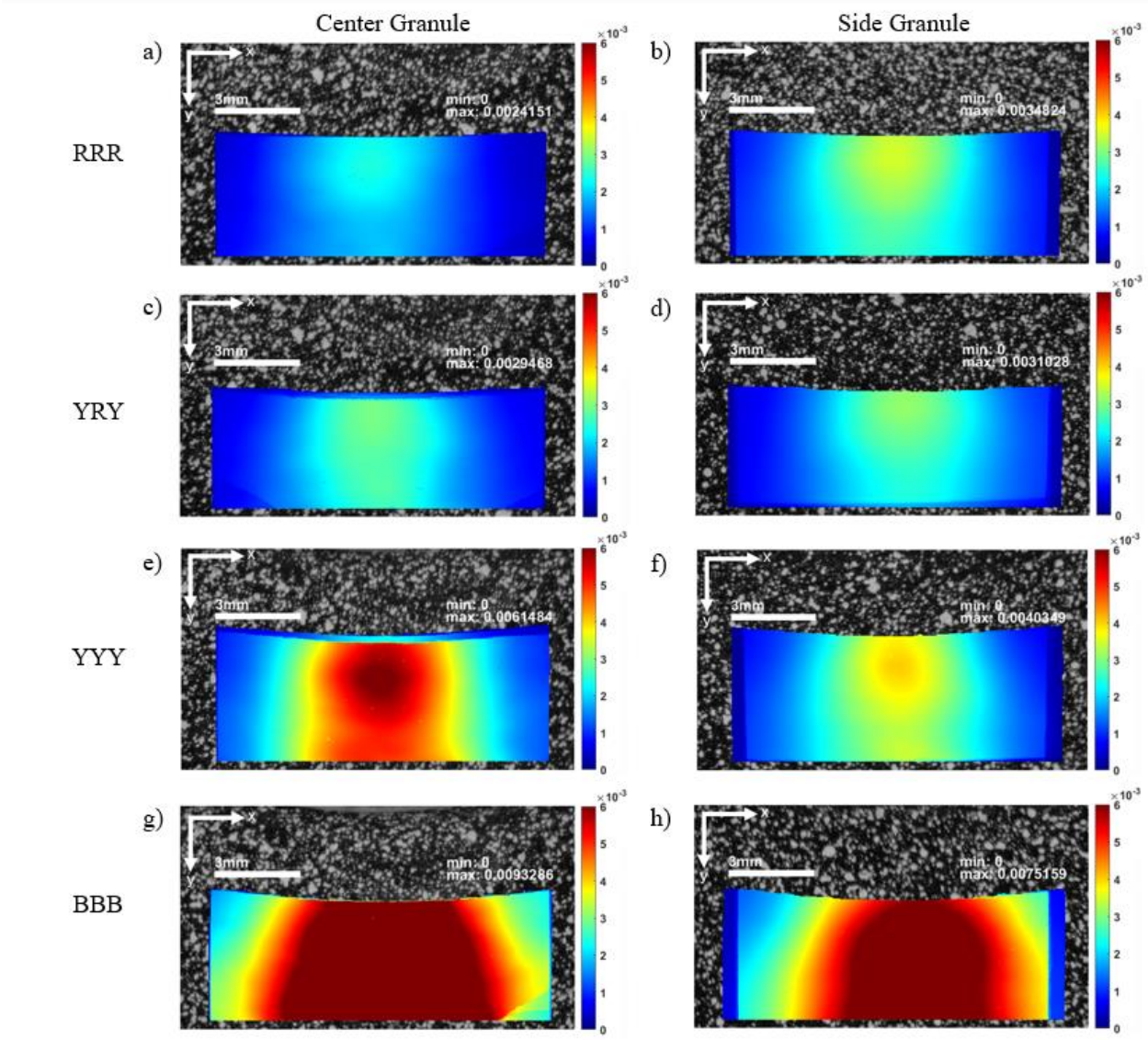

Figure 18 – Energy-like quantity fields (E) of the polymer at max compression for the granular media combinations tested. (a), (c), (e), (g) - *E* fields of the area under the center granule. (b), (d), (f), (h) – *E* fields of the averaged area under the side granules.

The magnitudes of the values are similar for the areas under the center and side granules for the RRR and YRY combinations. For the center granule, the RRR combination has a max E of $0.0024e^{-3}$ (Figure 18a) compared to $0.0029e^{-3}$ in the YRY combination (Figure 18c). The side

granule of the RRR combination has a higher max of $0.0034e^{-3}$ (Figure 18b) compared to $0.0031e^{-3}$ in the YRY combination (Figure 18d). However, the max values from these combinations are lower than the max values experienced by the YYY combination. As seen on Figure 18e, the area under the center granule has E localized in a circular shape under the point of contact with a max of $0.0061e^{-3}$. The same shape can be seen for the area under the side granule on Figure 18f with a max of $0.0040e^{-3}$. It is important to note that the magnitudes of the E are a magnitude of 10^{-4} less than the magnitudes of the strain components.

Results from Vakakis' s *et al*. computer model [5] display a higher E density on the outer pucks compared to the center puck (refer to Figure 1). This relationship is not observed for all granular media combinations, but it is true for the RRR and YRY combinations. The computer model and the apparatus discussed in this paper constrain the pucks in the x direction during impact. However, in the computer model the side constraints are in contact with the impact surface. In the physical experiments performed, there is a slight gap of 2mm between the side walls of the granular media holder and the polymer. It is possible that due to this gap and the high deformation of the PDMS elastomer during impact, the outermost granules displace outwards and part of the granule moves slightly under the side constraints. If the polymer was in contact with the granular media holder, it is possible that the polymer would still want to deform as it does during these trials, but now the wall constraints are restricting an area of the polymer from deforming and as a result the area around the side pucks experiences a higher stress and E density.

CHAPTER 4: CONCLUSIONS AND FUTURE WORK

4.1 Conclusions

An apparatus is built from a reference toy to accommodate and test combinations of granular media under an impact load. The apparatus is modified between trials and granules rearranged to reduce errors between trials. The wave propagation through the granular media is quantified through the strain observed in an impact polymer surface. ε_{xx}, ε_{yy}, and ε_{xy} strain fields were created through the implementation of DIC and ncorr software. A conversion from the strains found to E density is used to obtain the energy-like quantity fields. The resulting E and strain fields are compared to existing computer models. Although the experiments performed in this research closely resemble the computer model from Vakakis *et al*., the obtained data varies from the model in terms that the E experienced is not necessarily greater in the area under the outermost granules. Rather, a combination of the impact surface material and fixed boundary constraints affect the strain and E experienced around the area by the outermost granules.

There are inconsistencies between the strain experienced and the diameter of the pucks in contact with the polymer. In some scenarios, the RRR combination experiences less strain and in others the YRY combination experiences less strain. However, the addition of a middle row of granular media with a smaller diameter between the YYY and YRY sees significant change in the strain experienced. For all strains and energy-like quantities, the area under the center and side granules of the YRY combination experiences less strain than in the YYY combination despite having the same top and bottom rows of granules. It is possible that there are greater frictional effects experienced by the center row when a granule of smaller diameter compared to the neighboring top and bottom granules is used. Between the RRR and YYY combinations, it is

easily observed that reducing the diameter of the granules while maintaining the same number of total granules, rows, and contact granules reduces the strain and E that the impact polymer receives. Overall, the strain fields between the different puck combinations are similar and vary only by magnitude. There are symmetrical effects observed across the y axis where the point of contact occurs for all strain and E fields.

4.2 Future Work

The experiments performed for this research focus on performing DIC analysis on the impact surface (polymer) to find the displacements and strains experienced from the forces being experienced by the pucks. Expanding on the DIC applications, it would be interesting to use the software to analyze the effects of the strains experienced on the pucks. The experimental setup would change by having a rigid impact surface, and using pucks of varying diameters made from PDMS using the same methods by which the polymer was made and speckled from sections 2.4 and 2.5. The diameter of the pucks would have to vary between 0mm – 5mm so that the current camera frame is able to capture the movement of the speckles during impact between pucks. The same camera settings can be maintained to capture an image at the bottom most displacement.

However, improving the camera by purchasing a camera that can capture a higher framerate at the existing resolution would allow for clearer images of the speckle displacements and even the possibility of a series of images clear enough to analyze the change in strain experienced over time. Furthermore, keeping the idea of a movable setup and stationary camera, the whole granular-solid interface area can be imaged rather than just the area under the granules. Strain results in this paper were limited to the camera view dimensions. A larger field of view from a different camera might yield strain patterns further down the impact surface.

An improved apparatus should be designed to accommodate pucks without the pucks having to be glued together, while still preventing significant translation towards the camera during impact. In future experiments, the impacting block should be perfectly level from release till impact as to not impact the pucks at an angle. The current setup requires a granular media holder to be changed for every different granular media combination. The setup could be improved by having a door or hatch that easily allows for changing combinations, and transparent enough for the camera to capture the speckle movement. To hold different granular media sizes and row combinations, the setup should have an adjustable wall on both sides of the pucks, that can be moved around and locked in place to maintain the pucks in the same place during trials.

Experiments modeled in this report use fourteen granules in a 5-4-5 combination. It would be interesting to observe the strain effects on the impact surface based on a different number of layers and an increase in number of granules used. If solid pucks are used, machining the granules with tighter tolerances will lead to a decrease in error from granule dimensions. Using steel spherical granules and modeling the same experiment as this paper without gluing the top row might show different results that more accurately account for energy dissipation from rotational effects.

Future work could potentially calculate a balance of potential energy and strain energy of the system. It is possible that the total strain energy scales to the initial potential energy in some way. The energy experienced by the polymer would be expected to be significantly less than the potential energy from the compressed spring block system due to the frictional effects from the rotations, the energy mitigated in the time frame between the initial hit and the max compression frame, and frictional effects between the block and walls of the toy. In this thesis, the spring

coefficient in the spring block system is not calculated, and the energy balance is not compared for this system. However, if able to have a more accurate model (possibly in 3D) to account for all strains, it would be interesting to see a potential relationship between the potential energy and strain energy.

APPENDICES

APPENDIX A

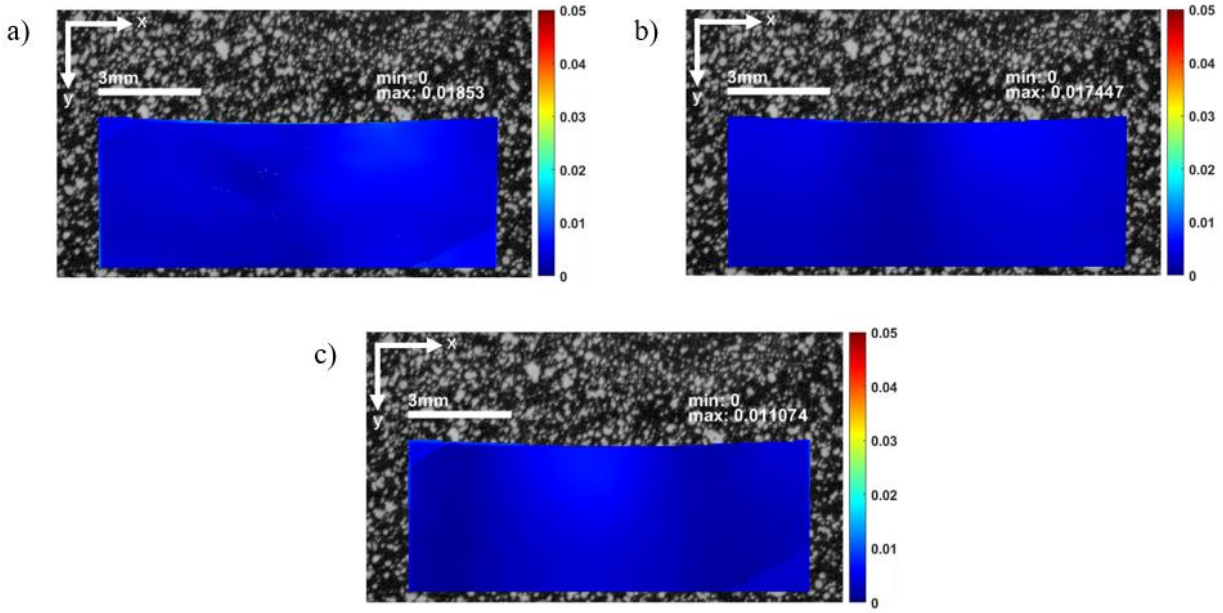

Figure A.1- Standard deviation fields corresponding to a) ε_{yy} , b) ε_{xx} , and c) $\varepsilon_{xy}$for the area under the center puck in the RRR combination.

REFERENCES

[1] Zhang, Z., Manevitch, L.I., Smirnov, V., Bergman, L.A., Vakakis, A.F.: *Extreme nonlinear energy exchanges in a geometrically nonlinear lattice oscillating in the plane*. J. Mech. Phys. Solids 110, 1–20 (2018)

[2] Zhang, Z., Koroleva, I., Manevitch, L.I., Bergman, L.A., Vakakis, A.F.: *Non-reciprocal acoustics and dynamics in the in-plane oscillations of a geometrically nonlinear lattice*. Phys. Rev. E 94(3), 032214 (2016)

[3] Melo, F., Job, S., Santibanez, F., Tapia, F.: *Experimental evidence of shock mitigation in a Hertzian tapered chain*. Phys. Rev. E 73(4), 041305 (2006)

[4] Lawney, B.P., Luding, S.: *Frequency filtering in disordered granular chains*. Acta Mech. 225, 2385–2407 (2014)

[5] Wang, C., Zhang, Q. & Vakakis, A.F. *Wave transmission in 2D nonlinear granular-solid interfaces, including rotational and frictional effects*. Granular Matter 23, 21 (2021)

[6] Lazaridi, A.N., Nesterenko, V.F.: *Observation of a new type of solitary waves in a one-dimensional granular medium*. J. Appl. Mech. Tech. Phys. 26(3), 405–408 (1985)

[7] Nesterenko, V.F.: *Propagation of nonlinear compression pulses in granular media*. J. Appl. Mech. Tech. Phys. 24, 733–743 (1983)

[8] Johnson, K.L.: *Contact Mechanics*. Cambridge University Press, Cambridge (1985)

[9] Starosvetsky, Y., Jayaprakash, K.R., Hasan, M.A., Vakakis, A.F.: *Topics on the Nonlinear Dynamics and Acoustics of Ordered Granular Media*. World Scientific Press, Singapore (2017)

[10] Wen Zhang, Jun Xu, *Quantitatively solitary wave tuning strategies based on one-dimensional cylindrical granular chains*, Extreme Mechanics Letters, Volume 40, 2020

[11] Job, S., Melo, F., Sokolow, A., Sen, S.: *How Hertzian solitary waves interact with boundaries in a 1D granular medium*. Phys. Rev. Lett. 94, 178002 (2005)

[12] Yang, J., Khatri, D., Anzel, P., Daraio, C.: *Interaction of highly nonlinear solitary waves with thin plates*. Int. J. Solids Struct. 49, 1463–1471 (2012)

[13] Potekin, R., McFarland, D.M., Vakakis, A.F.: *Nonlinear wave scattering at the flexible interface of a granular dimer chain*. Granul. Matter 15, 51–68 (2016)

[14] Zhang, Q., Potekin, R., Li, W., Vakakis, A.F.: *Nonlinear wave scattering at the interface of granular dimer chains and an elastically supported membrane*. Int. J. Solids Struct. 182–183(202001), 46–63 (2020)

[15] Yang, J., Sutton, M.: *Nonlinear wave propagation in a hexagonally packed granular channel under rotational dynamics*. Int. J. Solids. Struct. 77(3), 65–73 (2015)

[16] Goldenberg, C., Goldhirsch, I.: *Friction enhances elasticity in granular solids*. Nature 435, 188–191 (2005)

[17] Chattoraj, J., Gendelman, O., Ciamarra, M.P., Procaccia, I.: *Oscillatory instabilities in frictional granular matter*. Phys. Rev. Lett. 123, 098003 (2019)

[18] Charan H., Gendelman O., Procaccia I., Shefer Y. *Giant Amplification of Small Perturbations in Frictional Amorphous Solid*, arXiv:2001

[19] Zhen Zhao, Caishan Liu, and Bernard Brogliato. *Energy dissipation and dispersion effects in granular media*. Phys. Rev. E 78, 031307 – Published 22 September 2008

[20] Bourrier, F., Nicot, F. & Darve, F. *Physical processes within a 2D granular layer during an impact*. Granular Matter 10, 415–437 (2008)

[21] Andrea Leonard, Laurent Ponson, Chiara Daraio, *Wave mitigation in ordered networks of granular chains, Journal of the Mechanics and Physics of Solids*, Volume 73, 2014, Pages 103-117

[22] Leonard, A., Chong, C., Kevrekidis, P.G. et al. *Traveling waves in 2D hexagonal granular crystal lattices*. Granular Matter 16, 531–542 (2014)

[23] Sen, S., Hong, J., Bang, J., Avalos, E., Doney, R.: *Solitary waves in the granular chain*. Phys. Rep. 462(2), 21 (2008)

[24] Daraio, C., Nesterenko, V.F., Herbold, E.B., Jin, S.: Energy trapping and shock disintegration in a composite granular medium. Phys. Rev. Lett. 96(5), 058002 (2006)

[25] Spadoni, A., Daraio, C.: *Generation and control of sound bullets with a nonlinear acoustic lens*. P. Natl. Acad. Sci. USA 107(16), 7230 (2010)

[26] Hasan, M.A., Cho, S., Remick, K., McFarland, D.M., Vakakis, A.F., Kriven, W.M.: *Experimental study of nonlinear acoustic bands and propagating breathers in ordered granular media embedded in matrix.* Granular Matter 17, 49–72 (2015)

[27] Tramsen HT, Heepe L, Gorb SN. *Bioinspired Granular Media Friction Pad: A Universal System for Friction Enhancement on Variety of Substrates.* Biomimetics (Basel) (2022)

[28] Blaber J., Adair, B. and Antoniou A., "*Ncorr: Open-Source 2D Digital Image Correlation Matlab Software.*" Experimental Mechanics (2015)

[29] J P Lewis, "*Fast Normalized Cross-Correlation*." Industrial Light & Magic (1995)

[30] Clément Ernould, Benoît Beausir, Jean-Jacques Fundenberger, Vincent Taupin, Emmanuel Bouzy, Chapter Two - *Development of a homography-based global DIC approach for high-angular resolution in the SEM*, Editor(s): Martin Hÿtch, Peter W. Hawkes, Advances in Imaging and Electron Physics, Elsevier, Volume 223, 2022, Pages 49-73

[31] B Pan "Reliability-guided digital image correlation for image deformation measurement." Optical Society of America (2009)

[32] B Pan, H Xie, Z Guo and T Hua. *Full-field strain measurement using a two-dimensional Savitzky-Golay digital differentiator in digital image correlation*. Optical Engineering (2007)

[33] Toysmith. *Marbles Oh Snap 2.0*. Fat Brain Toys. Accessed at: https://www.fatbraintoys.com/toy_companies/toysmith/marbles_oh_snap_20.cfm

[34] Ariati R, Sales F, Souza A, Lima RA, Ribeiro J. *Polydimethylsiloxane Composites Characterization and Its Applications: A Review. Polymers* (Basel). 2021

[35] Marc P. Wolf, Georgette B. Salieb-Beugelaar, Patrick Hunziker, *PDMS with designer functionalities—Properties, modifications strategies, and applications*, *Progress in Polymer Science*, Volume 83, 2018, Pages 97-134